

## Misocyclone Characteristics along Florida Gust Fronts during CaPE

KATJA FRIEDRICH AND DAVID E. KINGSMILL

*NOAA-CIRES/Environmental Technology Laboratory, University of Colorado, Boulder, Colorado*

CARL R. YOUNG

*Desert Research Institute, Reno, Nevada*

(Manuscript received 16 February 2005, in final form 16 May 2005)

### ABSTRACT

Multiple-Doppler radar and rawinsonde data are used to examine misocyclone characteristics along gust fronts observed during the Convection and Precipitation/Electrification (CaPE) project in Florida. The objective of this study is to investigate the observational representativeness of previous numerical simulations of misocyclones by employing a consistent analysis strategy to 11 gust fronts observed in the same region. The investigation focuses on the intensity range of misocyclones and their organization along gust fronts; the relationship between misocyclone intensity and horizontal wind shear, vertical wind shear, and static stability; and the relationship between misocyclones and convection initiation.

The intensity of misocyclones, as indicated by the maximum values of vertical vorticity, varied from  $2.8 \times 10^{-3}$  to  $13.9 \times 10^{-3} \text{ s}^{-1}$ , although all but one case exhibited values less than  $6.4 \times 10^{-3} \text{ s}^{-1}$ . Organized misocyclone patterns were only found along small segments of gust fronts. Within those segments misocyclones were spaced between 3 and 7 km. Results show that the intensity of misocyclones was most closely related to the strength of horizontal wind shear across the gust front. The relationship between misocyclone intensity and vertical wind shear and static stability was not as clear. Although convection was initiated along the gust front in 7 of the 11 cases, those regions were not collocated with or in close proximity to misocyclones.

### 1. Introduction

Convection initiation often occurs nonuniformly along boundary layer convergence lines (hereafter also referred to as boundaries), which leads to difficulties in accurately nowcasting severe local storms. In some instances, these nonuniform convection patterns can be attributed to regional variations in thermodynamic stability, as has been observed in numerous studies (e.g., Purdom 1982; Mueller et al. 1993; Weckwerth et al. 1996). Kinematic variability along boundaries is also an important factor in convection initiation. For example, the shape of a coastline can affect the distribution of convective cloudiness along a sea-breeze front (Neumann 1951; Purdom 1976). Using a three-dimensional numerical model, Pielke (1974) found local vertical velocity maxima along the sea-breeze front where the

convex curvature in the coastline accentuated the convergence caused by the land-sea heating contrast. Another factor that can influence along-line kinematic variability is the interaction of horizontal convective rolls with boundaries. Wilson et al. (1992) showed that the points of intersection between a quasi-stationary, topographically forced boundary (in this case the Denver vorticity convergence zone) and horizontal convective rolls were favored regions of storm development. Wakimoto and Atkins (1994) and Atkins et al. (1995) observed enhanced cloud development in areas where horizontal convective rolls merged with sea-breeze fronts. Atkins et al. (1998) observed enhanced cloud development at the intersection points of horizontal convective rolls with a dryline.

Wave patterns or shearing instabilities in association with boundaries have also been observed to produce along-line variabilities. Carbone et al. (1990) observed that the vertices of a line-echo wave pattern (a series of 80–150-km-long arcs in radar reflectivity) along the length of a gust front were preferred regions of convec-

---

*Corresponding author address:* David Kingsmill, CIRES, 216 UCB, Boulder, CO 80309-0216.  
E-mail: David.Kingsmill@colorado.edu

tion development. Analysis of surface mesonet data from this study revealed local convergence maxima at these locations. Weckwerth and Wakimoto (1992) found gust front updraft maxima on the upshear (i.e., upward motion) side of Kelvin–Helmholtz waves that intersected the boundary 1–2 km above the surface at approximately 90° angles and 3–5-km intervals. Unfortunately, the data were not available to prove that storms initiated at these maxima. Kingsmill (1995) observed a series of small-scale (2–4 km) vertical vorticity maxima spaced at 3–5-km intervals along an intense gust front. Similar features have been observed by Carbone (1982, 1983), Mueller and Carbone (1987), Wakimoto and Wilson (1989), Wilson et al. (1992), Arnott et al. (2005), and Murphey et al. (2005), among others. Fujita (1981) has referred to these types of circulations as misocyclones. The misocyclones were hypothesized by Kingsmill (1995) to originate from a horizontal shearing instability, sometimes referred to as Helmholtz instability. Convergence and vertical velocity maxima were observed at locations adjacent to each of the vertical vorticity maxima. However, these were not preferred areas of convection development.

Lee and Wilhelmson (1997a,b) examined misocyclone development along numerically simulated thunderstorm outflow boundaries. They developed a conceptual model that summarizes the kinematic structure of this phenomenon. An adapted version of this model is shown in Fig. 1. Strong horizontal wind shear across the boundary triggers instabilities that intensify into centers of enhanced vertical vorticity, which we define as misocyclones. Inflections in the frontal boundary are one manifestation of the misocyclones. They also distort the horizontal wind field by producing local maxima of low-level convergence, indicated with circled plus signs, northwest and southeast of each circulation center. The locations of enhanced low-level convergence are also associated with enhanced upward motions and therefore are preferred areas for convection initiation. Lee and Wilhelmson (1997a, hereafter LW97a) proposed the optimal environment for strong misocyclone circulation as having strong across-front horizontal shear at the outflow leading edge, an ambient vertical shear profile of the depth similar to the outflow boundary and balanced with the cold pool circulation, and a neutrally stable environment through a layer considerably deeper than the outflow boundary.

The objective of our study is to investigate the observational representativeness of these numerical simulations. Previous observational studies of misocyclones (Carbone 1983; Mueller and Carbone 1987; Kingsmill 1995) have provided some guidance in addressing these issues, but they are lacking in a few key respects. First,

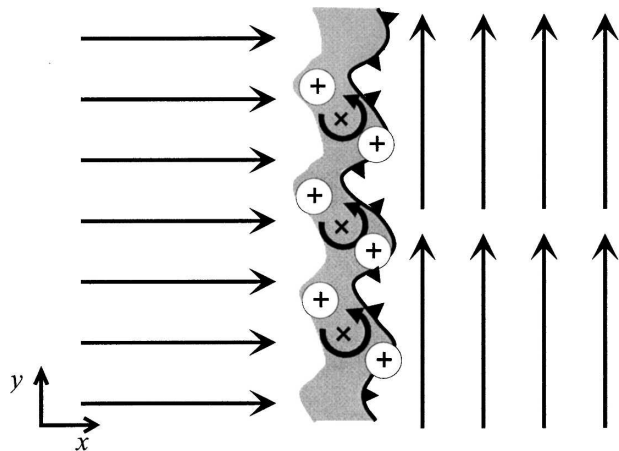


FIG. 1. Conceptual model of misocyclone circulations along the leading edge of a thunderstorm outflow based on results of Lee and Wilhelmson (1997a). Areas of enhanced positive vertical vorticity are indicated with crosses and areas of convergence with plus signs. The convergence zone is highlighted in gray.

they were all individual case studies focusing on different, but related, scientific topics. As a result, each study employed a different analysis strategy that was customized to address the topic of emphasis. Also, these observational cases studies occurred in three different regions within the United States (i.e., California, Colorado, and Florida), making the compositing of their results more complicated. To properly address these issues, a consistent analysis strategy needs to be employed on several cases that occurred within the same region. This is accomplished in this paper by examination of kinematic and thermodynamic structures along and adjacent to gust fronts observed during the Convection and Precipitation/Electrification (CaPE) project conducted in east-central Florida during the summer of 1991 (Wakimoto and Lew 1993). Eleven separate gust front cases are analyzed with multiple-Doppler radar-derived wind syntheses and balloon-borne thermodynamic and kinematic soundings. We focus on three main issues: 1) How often and to what degree do organized patterns of vertical vorticity and convergence occur along boundaries? 2) How often and to what degree do the optimal environmental conditions outlined by LW97a occur based on observational evidence? 3) Can the presence and intensity of misocyclones along a boundary be related to convection initiation?

Section 2 describes the observing systems used in this study and how their data were processed. Gust front and misocyclone characteristics are explored in section 3. The relationship between misocyclone strength and environmental characteristics such as horizontal wind shear, vertical wind shear, and static stability is exam-

ined in section 4. Section 5 discusses the influence of misocyclones on convection initiation. Finally, conclusions are presented in section 6.

## 2. Observing systems and data processing

The CaPE experiment operated in east-central Florida near Cape Canaveral during July and August 1991. More information on the CaPE experiment and its data sources can be found in Atkins et al. (1995), Frankhauser et al. (1995), Kingsmill (1995), Laird et al. (1995), Wakimoto and Kingsmill (1995), Yuter and Houze (1995), Weckwerth et al. (1996), Wilson and Megehardt (1997), Weckwerth (2000), and Kingsmill and Crook (2003) among other studies. The key observing systems used in this investigation are the CP3 and CP4 Doppler radar systems operated by the National Center for Atmospheric Research (NCAR) and the FL2 Doppler radar system sponsored by the Federal Aviation Administration (FAA). The locations of these C-band radars are shown in Fig. 2. Baselines between the radars were 23.2 km for CP3–CP4, 38.3 km for CP3–FL2, and 59.2 km for CP4–FL2. The investigation focused on 11 cases where gust fronts passed the study area while at least two radar systems were in operation. The locations of these gust fronts are indicated in Fig. 2, with those cases involving three radar analyses (CP3–CP4–FL2) in Fig. 2a and those cases involving two radar analyses (CP4–FL2 or CP3–FL2) in Figs. 2b and 2c, respectively.

One of the benefits afforded by using FL2 is a potentially larger domain for dual- or multiple-Doppler wind synthesis compared to the domain that would be possible if only CP3 and CP4 were used. However, the trade-off for this extended horizontal coverage is limited vertical coverage, since only the 0.5°-elevation surveillance scan data were available from FL2 in the directions east of its location. FL2 scanned at elevations above 0.5°, but only within narrow sectors west or north of its location, which are not suitable for this analysis. To complement these data, 0.3°-elevation surveillance scan data from CP3 and CP4 were utilized. With only one usable low-elevation angle scan from FL2 for wind synthesis, derivation of vertical winds was not possible for multiple-Doppler combinations involving FL2. Although volume data from CP3 and CP4 were available for determining vertical velocities, the area covered by the CP3–CP4 dual-Doppler lobes was not sufficient to provide information along the entire length of the gust fronts. Time differences between CP3, CP4, and FL2 surveillance scans were less than 1 min for any given wind synthesis volume. The number of analysis volumes available for each case varied between one (25

July) and five (5 and 15 August). Time intervals between successive wind synthesis volumes varied between 5 min (13 August) and 30 min (24 July), with an average of about 15 min.

Data were first edited to remove contamination from ground clutter, sidelobe, and second-trip echoes and to de-alias folded radial velocities. Individual surveillance scans employed in the analysis were then interpolated to a 600 m × 600 m Cartesian grid at 300 m AGL using a Cressman (1959) distance-dependent weighting scheme. Considering six independent grid points from the multiple-Doppler wind analysis (Carbone et al. 1985), the resolvable wavelength of motion is 3.6 km. Finally, horizontal wind fields were derived by multiple-Doppler radar synthesis using the method of least squares. When all three radars contributed to a synthesis, an overdetermined solution to the linear system of equations was employed. If only two radars contributed, a standard dual-Doppler solution was used. Analyses were constrained to an area where the standard deviation of horizontal winds was less than 5 m s<sup>-1</sup>, which corresponds to radar beam intersection angles between 20° and 170°.

Vertical profiles of kinematic and thermodynamic conditions in advance of the analyzed gust fronts were determined from Cross-Chain Loran Atmospheric Sounding Systems (CLASS) launched at Deer Park (DPK), Titusville (TCO), Orlando (ORL), and a mobile CLASS system (MCL) operated by NCAR as presented in Fig. 2. Most of the cases have a time differences between analysis and sounding launch of less than 40 min (with a variability of 2 min up to 4 h) and a spatial distance of less than 50 km (with a variability of 3–73 km). Time and spatial differences for each case are listed in Table 1.

## 3. Gust front and misocyclone characteristics

Gust fronts were primarily analyzed when completely disjointed from their parent thunderstorms (i.e., at least 5 km apart) and not close enough in proximity to interact with sea-breeze fronts approaching from the east (i.e., about 10 km apart). An example for the case on 13 August is provided in Fig. 3a. It shows a gust front together with the parent thunderstorm (left) and sea-breeze front (right) in a conventional west–east, south–north coordinate system.

The gust fronts examined in this study propagated mainly with an eastward component at 5 to 17 m s<sup>-1</sup> (Table 2). Gust fronts are defined as having a length of at least 10 km and are present for a minimum of 15 min (Wilson and Schreiber 1986). The average length of the analyzed gust fronts during CaPE ranges between

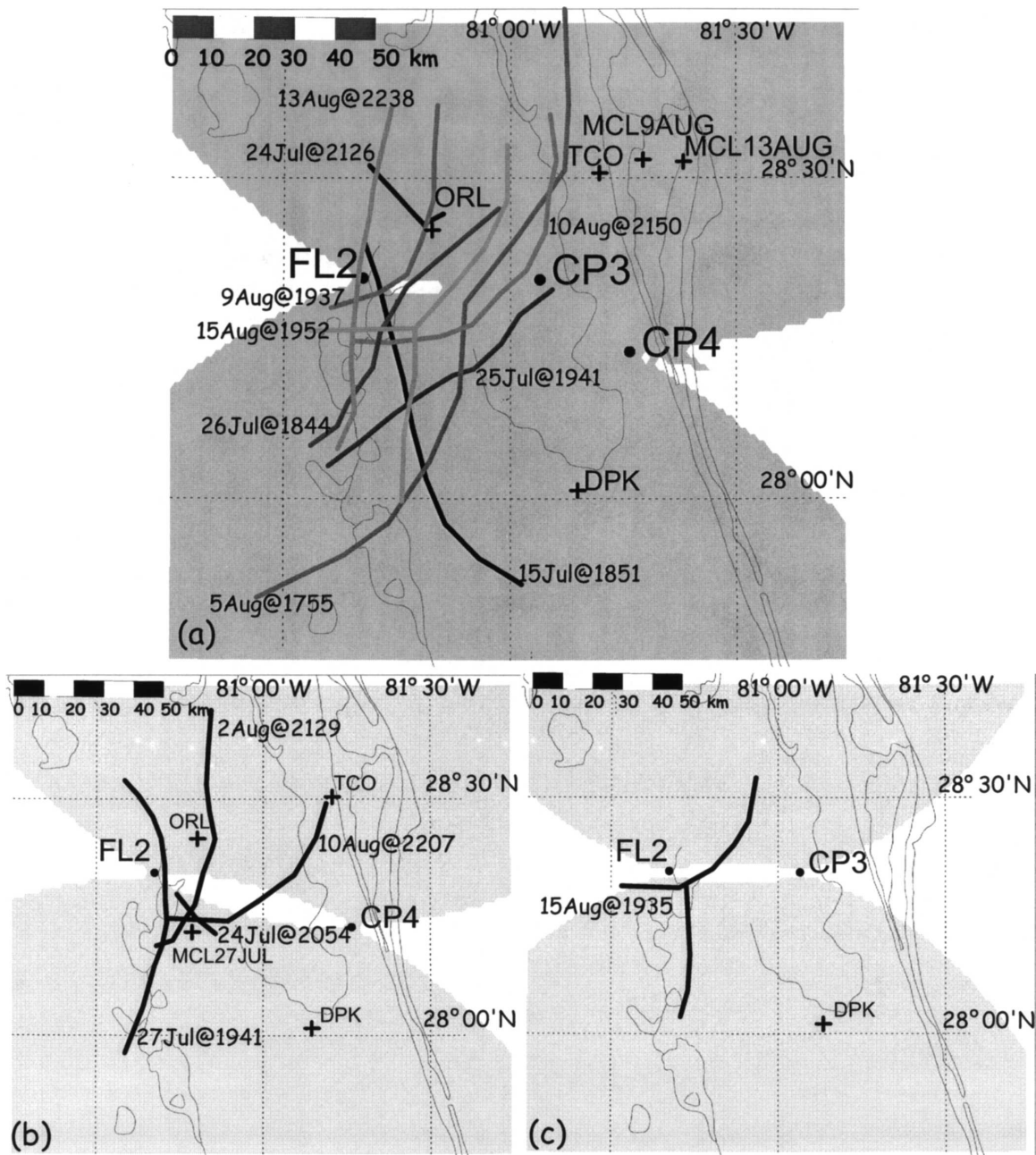


FIG. 2. The three different combinations of multiple-Doppler analysis employed in this study overlaid on maps of the investigation area with locations of Doppler radars (CP3, CP4, FL2) and rawinsonde sites (ORL, DPK, TCO, MCL) indicated by black-filled circles and plus signs, respectively: (a) CP3-CP4-FL2, (b) CP4-FL2, and (c) CP3-FL2. Traditional dual-Doppler analysis is applied in the light-gray-shaded areas, while the dark-shaded areas show locations where an overdetermined dual-Doppler solution is applied. The date, initial analysis time, and location of the 11 gust fronts examined are indicated, along with the date of each MCL rawinsonde.

27 and 100 km ( $\Delta y'$  in Table 2). The analysis of misocyclone characteristics is restricted to a 6-km-wide boxed region centered on the gust front (Figs. 3b and 3c). Wilson and Schreiber (1986) observed a convergence zone width range of 0.5 to 5.0 km in their Colorado-based study of boundaries. The center position for

each box was determined by examination of reflectivity and convergence fields.

The intensity and spatial distribution of misocyclones observed along gust fronts during CaPE varies greatly. Four characteristic examples are presented in Figs. 4 and 5. The strongest misocyclones were observed on

TABLE 1. Time and spatial differences between gust fronts and soundings: Differences between launching time and average analysis time ( $\Delta t$ ) and average distance between sounding location and gust front ( $\Delta x$ ) are shown.

Date	15 Jul	24 Jul	13 Aug	26 Jul	9 Aug	27 Jul	15 Aug	5 Aug	2 Aug	10 Aug	25 Jul
$\Delta t$ (hh:min)	1:57	4:10	0:10	0:02	0:03	0:10	1:03	0:07	0:38	0:02	0:18
$\Delta x$ (km)	28	3	73	55	52	7	44	40	45	11	59

15 July with values of vertical vorticity exceeding  $1 \times 10^{-2} \text{ s}^{-1}$  (Figs. 4a and 4b). Convergence along the gust front in this case was also quite strong, with maxima above  $1 \times 10^{-2} \text{ s}^{-1}$ . A large amount of horizontal wind

shear was evident across the boundary with southerly prefrontal winds of  $5\text{--}10 \text{ m s}^{-1}$  transitioning to southwesterly postfrontal winds of  $15\text{--}22 \text{ m s}^{-1}$ . Relative to the direction of propagation, postfrontal is defined as

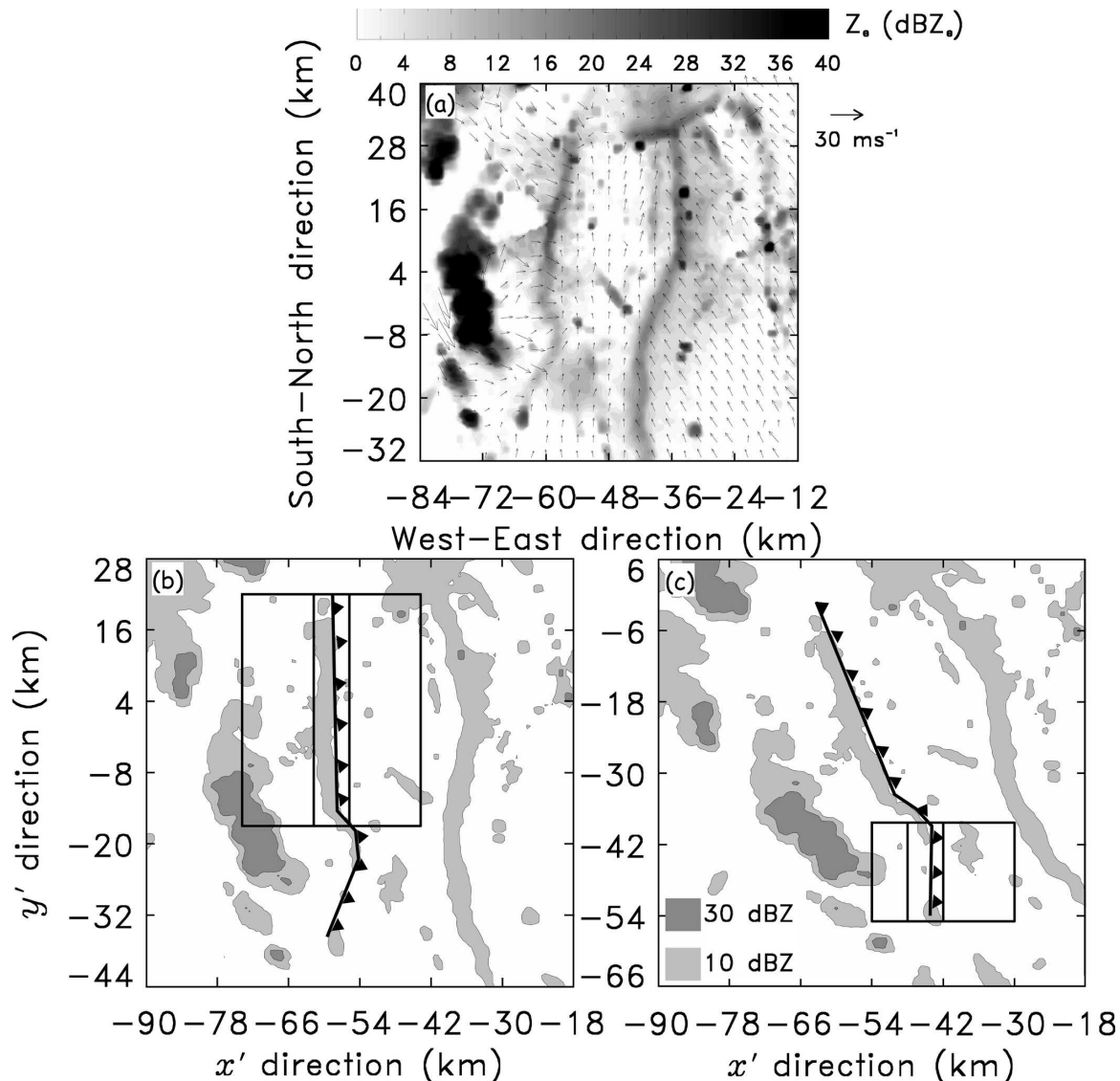


FIG. 3. (a) Horizontal wind field (arrows) at 312 m MSL overlaid on reflectivity factor field measured at 2238 UTC on 13 Aug. Grayscale for reflectivity is shown at top. Coordinate axes relative to the position of CP4. Wind vectors are plotted every 1.8 km (every third vector). (b) As in (a), but the original coordinate system is rotated counterclockwise by  $30^\circ$ . (c) As in (a), but rotated counterclockwise by  $12^\circ$ . In (b) and (c), areas containing reflectivity values greater than 10 and 30 dBZ are shaded light and dark gray, respectively. The sets of three rectangles in both panels indicate locations where analysis of the gust front (middle rectangle), postfrontal air mass (left rectangle), and prefrontal air mass (right rectangle) is focused. Bold line with barbs indicates the leading edge of the outflow boundary.

TABLE 2. Gust front and misocyclone characteristics: average analyzed gust front length ( $\Delta y'$ ), propagation speed and direction ( $\overline{UP}_{SPD}$ ,  $\overline{UP}_{DIR}$ ), average maximum vertical vorticity ( $\overline{\zeta}_{max}$ ), maximum vertical vorticity ( $\zeta_{max}$ ), average maximum convergence ( $\overline{CONV}_{max}$ ), and maximum convergence ( $CONV_{max}$ ). Cases are ordered as a function of misocyclone intensity ( $\overline{\zeta}_{max}$ ) and those with convection initiation are highlighted in bold.

Date	$y'$ (km)	$\overline{UP}_{SPD}$ ( $m\ s^{-1}$ )	$\overline{UP}_{DIR}$ ( $^{\circ}$ )	$\overline{\zeta}_{max}$ ( $10^{-3}\ s^{-1}$ )	$\zeta_{max}$ ( $10^{-3}\ s^{-1}$ )	$\overline{CONV}_{max}$ ( $10^{-3}\ s^{-1}$ )	$CONV_{max}$ ( $10^{-3}\ s^{-1}$ )
15 Jul	66.0	17.0	60	4.4	13.9	4.7	11.7
24 Jul	27.5	4.5	35	2.7	5.7	4.0	5.3
<b>13 Aug</b>	90.0	9.0	100	2.5	6.4	3.2	6.2
<b>26 Jul</b>	96.7	8.5	120	1.6	5.3	3.2	4.9
9 Aug	63.8	10.0	115	1.5	5.5	2.1	4.7
<b>27 Jul</b>	40.0	7.0	95	1.5	4.0	1.8	4.6
<b>15 Aug</b>	99.0	7.0	130	1.4	4.1	2.4	4.3
5 Aug	98.0	7.0	114	1.1	3.4	1.2	3.9
<b>2 Aug</b>	88.3	4.5	115	1.0	3.0	1.0	2.6
<b>10 Aug</b>	70.0	6.0	105	1.0	2.8	1.7	3.1
<b>25 Jul</b>	90.0	9.0	330	0.7	2.8	2.2	4.5

the area behind the gust front region, while prefrontal covers the area ahead of the gust front. Distinct but somewhat lower-magnitude vertical vorticity and convergence structures were also apparent on 13 August (Figs. 4c and 4d). The wind direction still veered from south to west, but the difference in speed across the boundary was smaller with prefrontal values of 6–9  $m\ s^{-1}$  and postfrontal values of 9–12  $m\ s^{-1}$ .

An example of a few misocyclones with relatively weak intensities occurred on 27 July (Figs. 5a and 5b). Not only were vertical vorticity and convergence magnitudes lower than the aforementioned cases ( $2 \leq CONV \leq 4 \times 10^{-3}\ s^{-1}$ ;  $\zeta \geq 2 \times 10^{-3}\ s^{-1}$ ), but the spatial distribution of misocyclones and the relative position of nearby convergence maxima were much more disorganized. Wind speeds were also much smaller, with prefrontal magnitudes of 1–3  $m\ s^{-1}$  and postfrontal magnitudes of 5–8  $m\ s^{-1}$ . Occurrence of a single misocyclone on 2 August is illustrated in Figs. 5c and 5d. Only one weak misocyclone with values of  $\zeta$  slightly above  $2 \times 10^{-3}\ s^{-1}$  developed in the southern part of the boundary with a small area of enhanced convergence ( $>2 \times 10^{-3}\ s^{-1}$ ) nearby to its north. Wind speed and direction differences across the boundary were very small.

As illustrated in Figs. 4 and 5, most gust fronts displayed variations in curvature along their length, making it difficult to use a single coordinate system for characterizing the properties of airflow orthogonal and parallel to the boundaries. To address this issue, gust fronts were usually subdivided into quasi-linear segments with distinctly different orientations. Each defined segment was rotated so that its  $y'$  axis was parallel and  $x'$  axis was orthogonal to the gust front.

An example of this procedure for the case on 13 August is provided in Figs. 3b and 3c. Detailed analysis

of the gust front occurred in the context of two segments: a 48-km-long segment to the south oriented  $12^{\circ}$ – $192^{\circ}$  and an 18-km-long segment to the north oriented  $30^{\circ}$ – $210^{\circ}$ . Each of these segments was rotated counterclockwise,  $12^{\circ}$  for the northern segment (Fig. 3b) and  $30^{\circ}$  for the southern segment (Fig. 3c), to place the gust front parallel to the  $y'$  axis.

Figures 6 and 7 present close-up views of the vertical vorticity and convergence distributions along the 15 July and 13 August gust front cases, respectively. Note that the coordinate systems in these figures have been rotated in a manner such that they are aligned with the boxes (A–D) shown in Fig. 4. A trait that becomes more clear in this zoomed-in perspective is the presence of inflections or waves in the convergence field along the gust fronts (see also reflectivity fields in Figs. 4 and 5), especially in the vicinity of misocyclones.

Misocyclones were spaced at regular but differing intervals in three of the four boundary segments. The southern segment B on 15 July (Fig. 6b), close in time and space to the analysis of Kingsmill (1995), exhibited misocyclone spacing of about 4 km, consistent with the Kingsmill study. Misocyclone spacing on 13 August varied from 5–6 km for the southern segment D (Fig. 7b) to 6–7 km for the northern segment C (Fig. 7a). In contrast, misocyclone spacing for the northern segment A on 15 July (Fig. 6a) was quite irregular, with two closely spaced ( $\sim 3$  km) circulations in the southern portion of the segment A separated by about 17 km from the next nearest circulation in the northern portion of the segment A.

The position of convergence maxima relative to misocyclones was much less organized. Many misocyclones did not have obvious convergence maxima nearby, and those that did showed no consistent pattern. Some convergence maxima were north (in the ro-

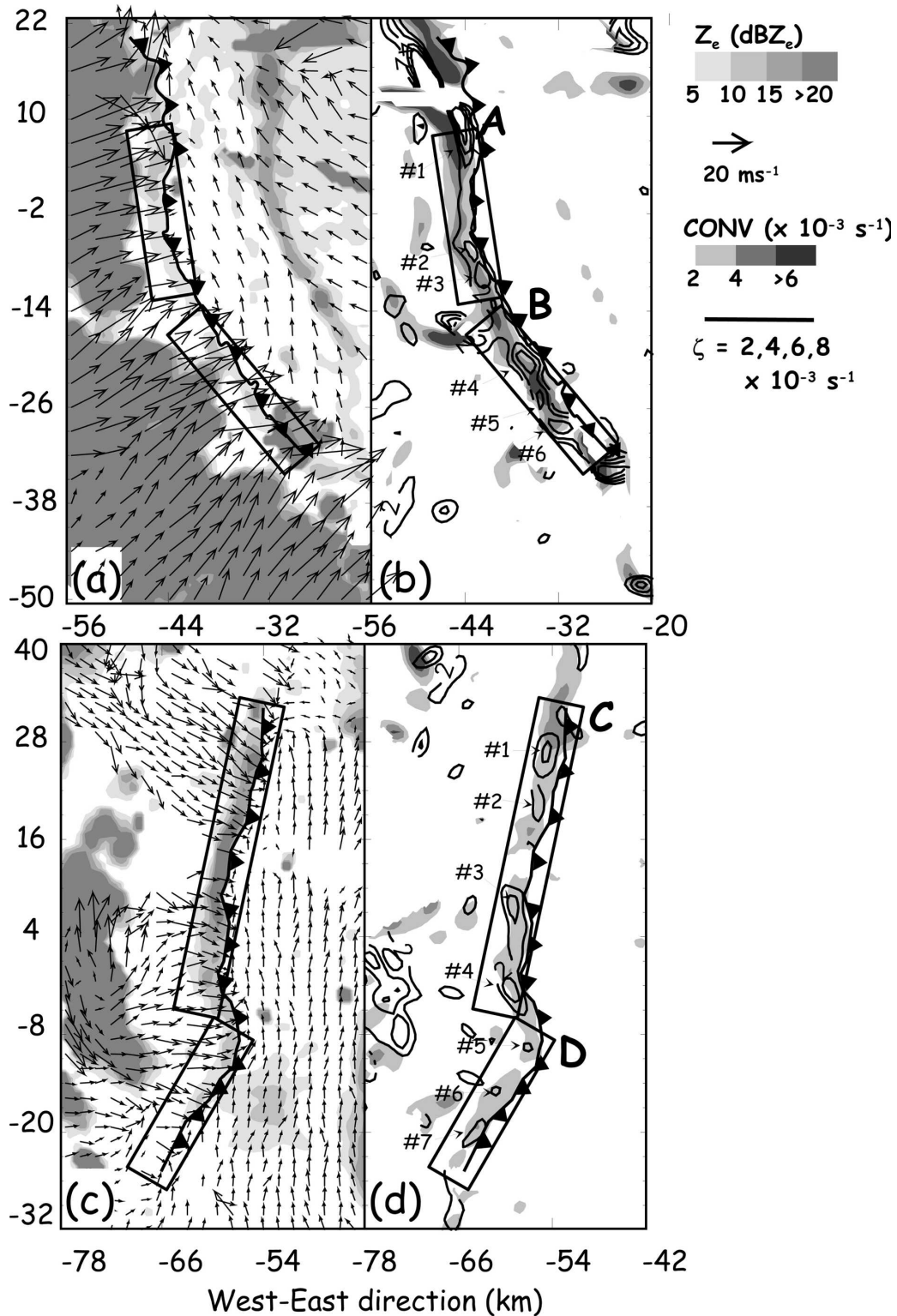


FIG. 4. Horizontal cross section of multiple-Doppler-derived data at 312 m MSL at (a), (b) 1859 UTC on 15 Jul and (c), (d) 2234 UTC on 13 Aug illustrating strong misocyclone intensities along the leading edge of thunderstorm outflows. In (a) and (c), horizontal wind fields (arrows) are overlaid on gray-shaded reflectivity (scale on the right). Wind vectors are plotted every 3 km (every fifth vector) in (a) and every 1.8 km (every third vector) in (c). (b) and (d) contain positive vertical vorticity (black contours) together with gray-shaded convergence (scale on the right). Misocyclones are numbered. The boxed regions labeled as A, B, C, and D represent the size of analyzed segments, and the leading edge of the gust front is illustrated by a solid line with barbs.

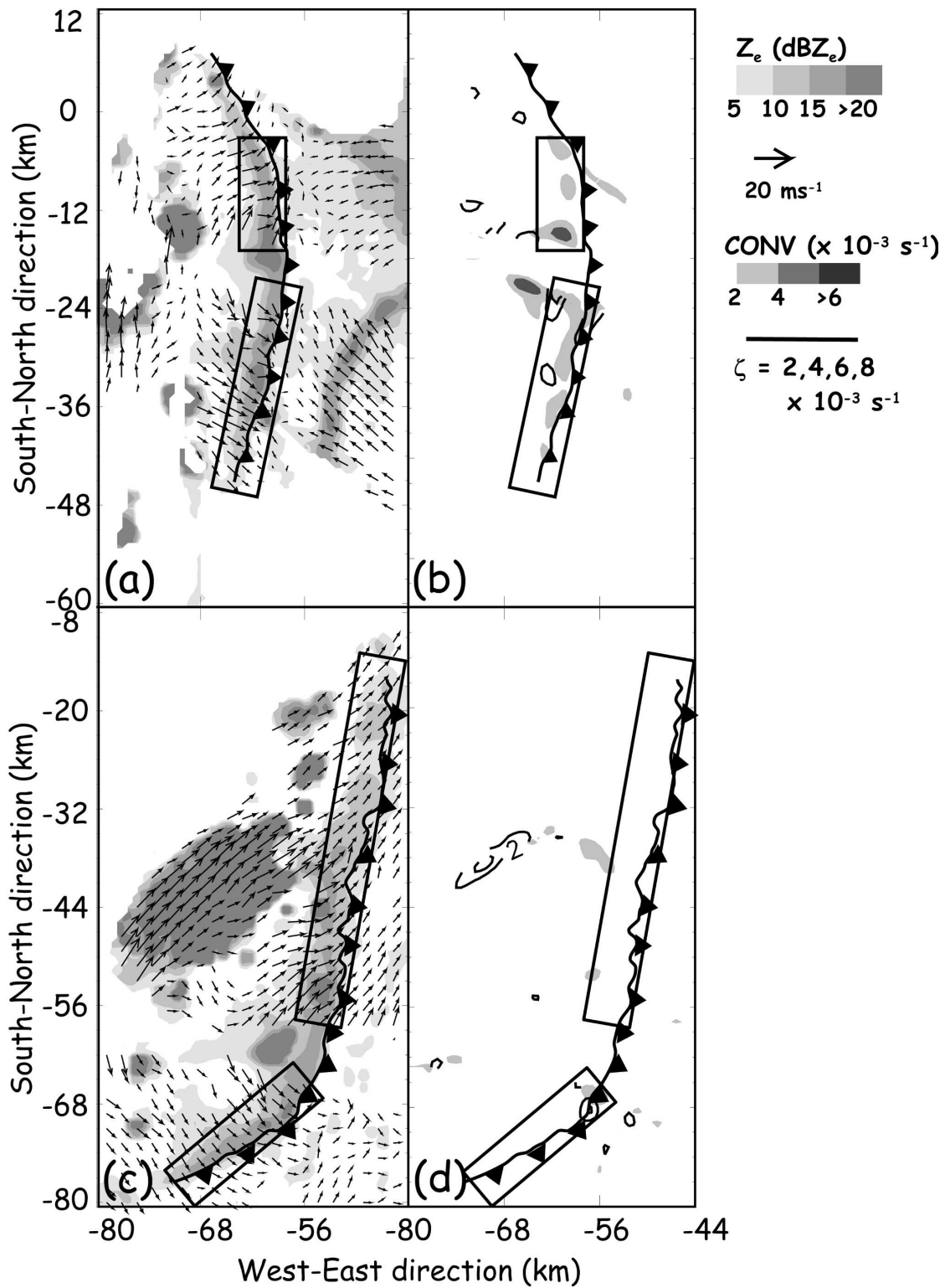


FIG. 5. As in Fig. 4, but illustrating weak misocyclone intensity at (a), (b) 15 UTC on 27 Jul and (c), (d) 2129 UTC on 2 Aug along the leading edge of thunderstorm outflows. In (a) and (c) wind vectors are plotted every 1.8 km (every third vector).

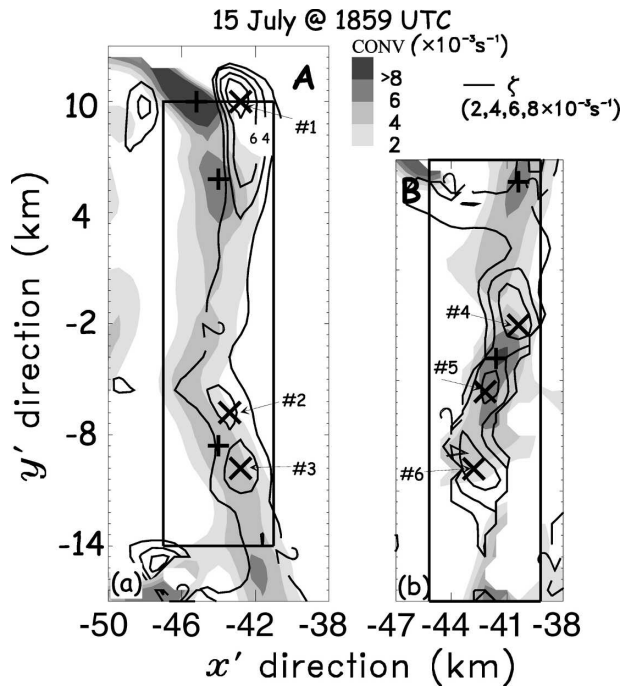


FIG. 6. Close-up view of the (a) northern segment A and (b) southern segment B in Figs. 4a and 4b at 1859 UTC on 15 Jul. The spatial distribution of convergence (gray shades) and positive vertical vorticity (black, solid lines) along the gust front are presented. Locations of vertical vorticity maxima greater than  $4 \times 10^{-3} \text{ s}^{-1}$  and convergence maxima greater than  $4 \times 10^{-3} \text{ s}^{-1}$  are labeled with crosses and plus signs, respectively. The 6-km-wide convergence zone is indicated by a black rectangle. Numbering of misocyclones according to Figs. 4a and 4b.

tated coordinate system framework) of misocyclones, some south, some both north and south, while others were nearly collocated. It is not clear to what degree the inconsistent pattern of convergence maxima and misocyclone location can be attributed to the relatively coarse resolution of the Doppler wind synthesis or the relatively elevated analysis height of 300 m. For the 15 July case, Kingsmill (1995) resolved convergence maxima ( $>8 \times 10^{-3} \text{ s}^{-1}$ ) located north of each misocyclone at 100 m MSL at 1907 UTC. Although the same locations of misocyclones were resolved in our study, a convergence maximum northeast of each location was only analyzed for misocyclones 3 and 5 in Fig. 6.

Vertical vorticity characteristics for each of the 11 gust front cases examined in this study are presented in Table 2. Two parameters were tracked within 6-km-wide rectangles that straddle each boundary segment: the maximum vertical vorticity,  $\zeta_{\text{max}}$ , and the average maximum vertical vorticity,  $\bar{\zeta}_{\text{max}}$ . The latter is determined by finding the maximum vertical vorticity along each cross section running orthogonal to the boundary

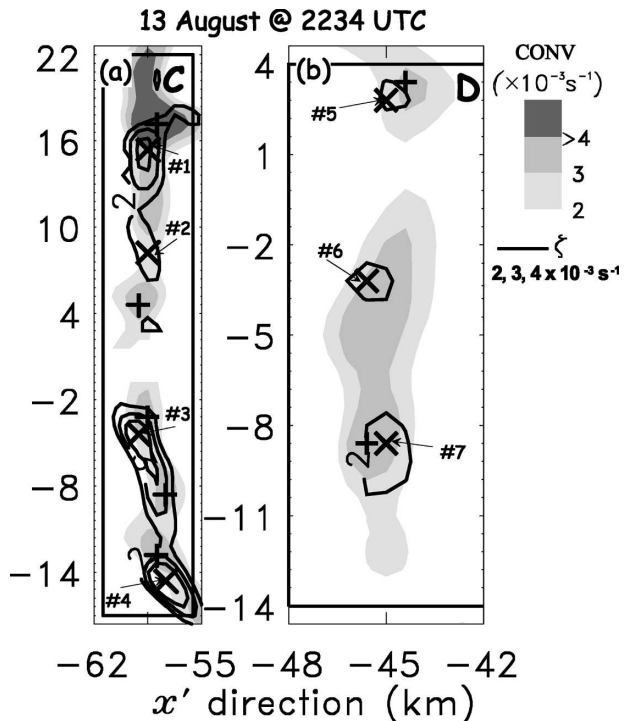


FIG. 7. As in Fig. 6, but for the (a) northern segment C and (b) southern segment D of Figs. 4c and 4d at 2234 UTC on 13 Aug. Locations of vertical vorticity maxima greater than  $4 \times 10^{-3}$  and  $2 \times 10^{-3} \text{ s}^{-1}$  are indicated with crosses in (a) and (b), respectively. Convergence maxima greater than  $3 \times 10^{-3} \text{ s}^{-1}$  are indicated with plus signs in both panels. Numbering of misocyclones according to Figs. 4c and 4d.

and then calculating the mean of these values. Parameters in Table 2 were derived by averaging the values obtained for each boundary segment analyzed for a particular case. Thus, small-scale variations and peak values are smoothed resulting in low  $\bar{\zeta}_{\text{max}}$  compared to values occurring with individual misocyclones.

Misocyclones are defined as vertical vorticity maxima having a spatial dimension smaller than 4 km (Fujita 1981). The resolvable strength of misocyclones is dependent on the spatial resolution of the observations. Kingsmill (1995) observed misocyclones with vertical vorticities of  $4\text{--}14 \times 10^{-3} \text{ s}^{-1}$  along the gust front on 15 July with a resolvable wavelength of 2.4 km. Values of  $\zeta$  varying between 10 and  $50 \times 10^{-3} \text{ s}^{-1}$  were derived by Mueller and Carbone (1987) for misocyclones along a gust front observed with a resolvable wavelength of 1.2 km. The magnitude of vertical vorticity maxima in their study is comparable to vertical vorticity maxima magnitudes found in numerical simulations having a grid resolution of 100 m (see, e.g., Fig. 9 in Lee and Wilhelmson 1997a). Misocyclones along a cold front with  $2 \leq \zeta \leq 12 \times 10^{-3} \text{ s}^{-1}$  were observed by Arnott and

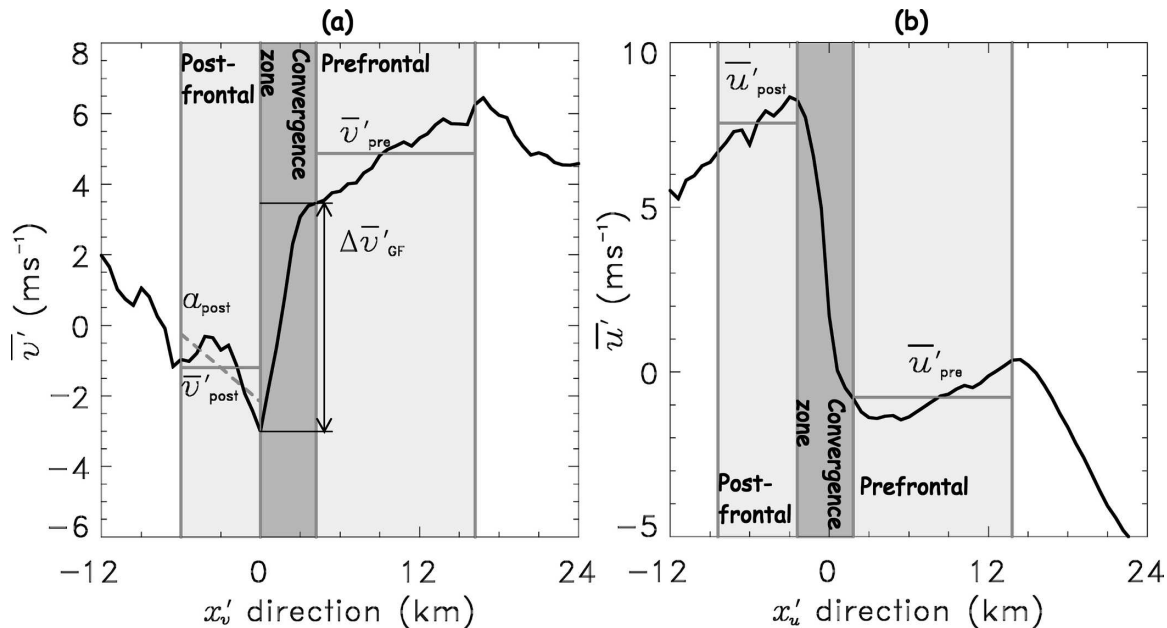


FIG. 8. Segmental average of the (a) alongfront wind velocity ( $v'$ ) across the gust front ( $x'_v$  direction) and (b) across-front wind velocity ( $u'$ ) across the gust front ( $x'_u$  direction). The profiles represent the mean values of the northern segment at 2238 UTC on 13 Aug 1991. Horizontal wind shear parameters are denoted by  $\overline{u'_{\text{post}}}$ ,  $\overline{u'_{\text{pre}}}$ ,  $\overline{v'_{\text{post}}}$ , and  $\overline{v'_{\text{pre}}}$ . The anticyclonic shear in the postfrontal area is denoted by  $a_{\text{post}}$ . The difference between  $\overline{v'}$  at the edges of the convergence zone is denoted by  $\Delta \overline{v'_{\text{GF}}}$ . See text for further explanations of those parameters.

Richardson (2004) with a resolvable wavelength of 0.6 km. Using the same high resolution, Marquis and Richardson (2004) determined  $\zeta$  values of  $4\text{--}20 \times 10^{-3} \text{ s}^{-1}$  along a dryline. Although lower values of vertical vorticity occurred in our study, which might be caused by a coarser horizontal resolution, trends and implications of misocyclone characteristics on the environmental wind field can still be derived to address the three main issues of this paper.

To address the representativeness of the numerical model results in a clear way, we sorted the 11 gust front cases according to their average maximum vertical vorticity values (Table 2). Most of the cases exhibited average maximum vertical vorticities below  $1.6 \times 10^{-3} \text{ s}^{-1}$  and maximum vertical vorticity below  $5.5 \times 10^{-3} \text{ s}^{-1}$ . Distinct vertical vorticity and convergence structures were observed on 15 July, 24 July, and 13 August with values of  $\overline{\zeta}_{\text{max}} \geq 2.5 \times 10^{-3} \text{ s}^{-1}$  and  $\zeta_{\text{max}} \geq 5.7 \times 10^{-3} \text{ s}^{-1}$ .

Maximum convergence ( $\text{CONV}_{\text{max}}$ ) and average maximum convergence ( $\overline{\text{CONV}}_{\text{max}}$ ) were determined in the same manner as  $\zeta_{\text{max}}$  and  $\overline{\zeta}_{\text{max}}$  and are also listed in Table 2. Convergence magnitude is closely linked with vertical vorticity magnitude; strong misocyclones are associated with higher-magnitude convergence and vice versa.

#### 4. Relationship between misocyclones and environmental characteristics

The relationship between misocyclones and horizontal wind shear, vertical wind shear, and static stability is examined in this section as a means to assess the validity of the optimal environment for misocyclone development proposed by LW97a.

##### a. Horizontal wind shear

This investigation focuses on the analysis of horizontal wind shear across the gust front in relation to misocyclone strength. All calculations are based solely on the horizontal wind vector derived from multiple-Doppler radar measurements. A detailed description about the determination of the horizontal wind shear parameters is given in appendix A.

Horizontal wind shear across the boundary is investigated based on the across- and alongfront wind velocities within the rotated coordinate system (denoted as  $u'$  and  $v'$  components) derived for each segment and averaged over all segments of a certain analysis time (temporal averaging) and over all analysis times (case averaging). The alongfront wind shear is expressed by the mean pre- and postfrontal wind velocities referred to as  $\overline{v'_{\text{pre}}}$  and  $\overline{v'_{\text{post}}}$ , respectively (Fig. 8a) and the dif-

TABLE 3. Horizontal wind shear parameters derived from the case-average profiles of the across-front ( $u'$ ) and alongfront ( $v'$ ) wind speeds: mean pre- and postfrontal, alongfront wind velocities ( $\overline{v'_{pre}}$ ,  $\overline{v'_{post}}$ ), and the mean pre- and postfrontal, across-front wind components, ( $\overline{u'_{pre}}$ ,  $\overline{u'_{post}}$ ). Differences between  $\overline{v'_{pre}}$  and  $\overline{v'_{post}}$  are denoted as  $\overline{v'_{pre-post}}$ , while differences between  $\overline{u'_{post}}$  and  $\overline{u'_{pre}}$  are denoted as  $\overline{u'_{post-pre}}$ . The amount of anticyclonic shear on the postfrontal edge of the gust front is represented by  $a_{post}$ , while the velocity difference within the convergence area is represented by  $\Delta\overline{v'_{GF}}$ . Case ordering and bold highlighting as in Table 2.

Date	$\overline{u'_{post}}$ ( $\text{m s}^{-1}$ )	$\overline{v'_{pre}}$ ( $\text{m s}^{-1}$ )	$\overline{v'_{post}}$ ( $\text{m s}^{-1}$ )	$\overline{u'_{pre}}$ ( $\text{m s}^{-1}$ )	$\overline{u'_{post-pre}}$ ( $\text{m s}^{-1}$ )	$\overline{v'_{pre-post}}$ ( $\text{m s}^{-1}$ )	$a_{post}$ ( $\text{m s}^{-1} \text{ km}$ )	$\Delta\overline{v'_{GF}}$ ( $\text{m s}^{-1}$ )
15 Jul	18.4	6.0	0.2	1.1	17.3	5.8	-6.1	10.1
24 Jul	14.2	4.1	-6.4	2.6	11.6	10.5	8.7	7.4
<b>13 Aug</b>	6.8	4.8	0.8	-1.0	7.8	4.0	-3.3	4.9
<b>26 Jul</b>	8.9	3.1	2.4	-0.3	9.2	0.7	-4.2	2.5
9 Aug	9.4	-0.4	-1.4	3.6	5.8	1.0	-6.3	3.1
<b>27 Jul</b>	2.9	1.6	-0.1	-0.4	3.3	1.7	-1.1	3.1
<b>15 Aug</b>	7.8	2.4	0.5	0.5	7.3	1.9	-2.1	3.2
5 Aug	4.6	2.0	-0.7	2.4	2.2	2.7	0.9	2.1
<b>2 Aug</b>	5.4	3.5	1.5	1.3	4.1	2.0	-1.4	1.9
<b>10 Aug</b>	4.3	3.4	1.8	-0.5	4.8	1.6	0.7	2.0
<b>25 Jul</b>	6.6	-0.9	-1.5	1.8	4.8	0.6	1.4	0.8

ferences, denoted as  $\overline{v'_{pre-post}}$ . In the same way, pre- and postfrontal, across-front wind components,  $\overline{u'_{pre}}$  and  $\overline{u'_{post}}$  (Fig. 8b), and the differences,  $\overline{u'_{post-pre}}$ , are derived. The case-averaged horizontal wind shear parameters are presented in Table 3. They are sorted according to their misocyclone strength based on  $\tilde{\zeta}_{max}$  in Table 2. Horizontal profiles of the case-averaged  $v'$  and  $u'$  wind components across the boundary ( $x'_v$  and  $x'_u$  direction) are illustrated in Figs. 9 and 10.

According to the conceptual model in Fig. 1, strong horizontal wind shear across the boundary triggers instability. In this model, strong horizontal wind shear is present when postfrontal outflow air has no alongfront wind component while winds with only an alongfront component are observed in the prefrontal area ahead of the gust front (LW97a). The relationship between horizontal wind shear and instability is reflected in the observational data. By far the largest values of  $\overline{u'_{post}}$  and  $\overline{v'_{pre}}$  occurred on 15 July, 24 July, and 13 August (Table 3; Figs. 9 and 10, left panels). The postfrontal across-front wind component,  $\overline{u'_{post}}$ , is on average  $12.6 \text{ m s}^{-1}$ , and the prefrontal alongfront wind components,  $\overline{v'_{pre}}$ , is on average  $5.1 \text{ m s}^{-1}$  (Table 3). Horizontal wind shear is much less pronounced in the other cases where  $\tilde{\zeta}_{max} < 2 \times 10^{-3} \text{ s}^{-1}$  with average values of  $\overline{v'_{pre}} = 1.3 \text{ m s}^{-1}$  and  $\overline{u'_{post}} = 6.2 \text{ m s}^{-1}$ . To quantify the deviation of the observational wind fields relative to the conceptual model in Fig. 1, components orthogonal to  $\overline{u'_{post}}$  and  $\overline{v'_{pre}}$ , denoted as  $\overline{v'_{post}}$  and  $\overline{u'_{pre}}$ , are also analyzed. For all cases the margin of  $\overline{v'_{post}}$  ranges mainly between about  $-1.5$  and  $2.4 \text{ m s}^{-1}$  except for 24 July, where  $\overline{v'_{post}} = -6.4 \text{ m s}^{-1}$ . The prefrontal across-front component,  $\overline{u'_{pre}}$ , varies mainly between  $-1.0$  and  $3.6 \text{ m s}^{-1}$  (Table 3; Figs. 9 and 10). As a result,  $\overline{v'_{post}}$  and  $\overline{u'_{pre}}$  components in the observational data are small com-

pared to their orthogonal counterparts. Nevertheless, these small variations can influence the triggering of instabilities, leading to more irregular patterns of misocyclones and convergence maxima relative to the conceptual model.

The horizontal profile of  $\overline{u'}$  and  $\overline{v'}$  across the boundary, illustrated in Figs. 9 and 10, depicts the influence of horizontal wind shear on misocyclone strength. The largest values of  $\overline{v'_{pre-post}}$  occur for the cases with the strongest misocyclone intensity on 15 July, 24 July, and 13 August (see Fig. 9 left panel;  $\overline{v'_{pre-post}}$  in Table 3). Cases showing weaker misocyclone intensity have  $\overline{v'_{pre-post}}$  values below  $2.7 \text{ m s}^{-1}$  (middle and right panels in Fig. 9; Table 3).

The preceding results suggest that cases with strong horizontal wind shear across the boundary are associated with stronger misocyclones. Those findings agree with the numerical model results of LW97a, where horizontal shearing instabilities along the leading edge of thunderstorm outflows were shown to be strongly influenced by the magnitude of horizontal wind shear across the boundary. They observed vertical vortex sheet development in regions of strong horizontal shear with no boundary-parallel wind component within the outflow and a large component within the encountered prefrontal environment. Based on numerical model results, LW97a concluded that the horizontal shear instability dominates over the lobe-and-cleft pattern, when in the model, initial condition  $\overline{v'_{pre-post}}$  exceeds  $5 \text{ m s}^{-1}$ . Note that the value of  $\overline{v'_{pre-post}} > 5 \text{ m s}^{-1}$  is only exceeded on 15 and 24 July.

Some of the segmentally averaged  $v'$  components showed an anticyclonic shear in the postfrontal area close to the convergence zone ( $-6 \leq x'_v \leq 0 \text{ km}$  in the left and middle panels in Fig. 9). This supports the hy-

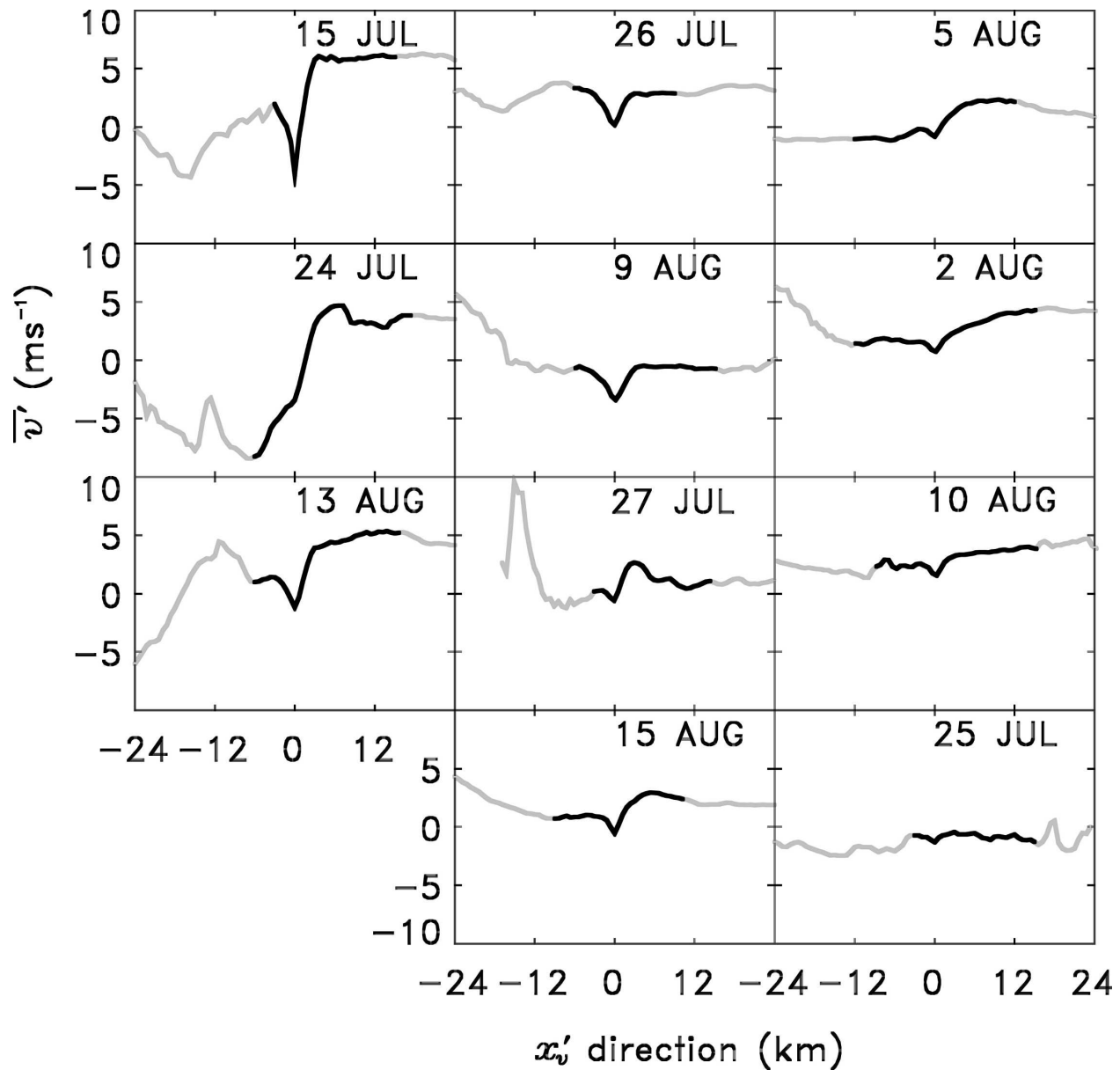


FIG. 9. Horizontal profiles of the case-averaged, alongfront wind velocity  $v'$  (gray line) across the gust front ( $x'$  direction). Cases are sorted according to  $\bar{\zeta}_{\max}$  in Table 2 starting with the upper-left panel proceeding downward for each column. The black line represents the area where the statistical analysis is applied.

pothesis by LW97a that misocyclones have a strong influence on the horizontal wind field at the leading edge of the boundary. In their simulations the misocyclones impart an anticyclonic shear to the postfrontal flow on the south side of their center locations. Likewise, the misocyclones impart a cyclonic shear to the prefrontal flow on the north side of their center locations (Fig. 1). When rotating each gust front segment to be parallel to its  $y'$  axis in our analysis, the east–west axis of the coordinate system is oriented mostly parallel to the out-

flow wind direction. Thus, the modification in the alongfront wind component caused by the misocyclone is revealed by an anticyclonic shear within the convergence zone. This shear is investigated based on the  $v'$  component in the postfrontal vicinity of and within the convergence zone (Fig. 8a). Note that the width of the convergence zone is determined for each segment separately because it is variable in time and space. A description of the methodology is given in appendix A. This phenomenon is quantified for all cases by applying

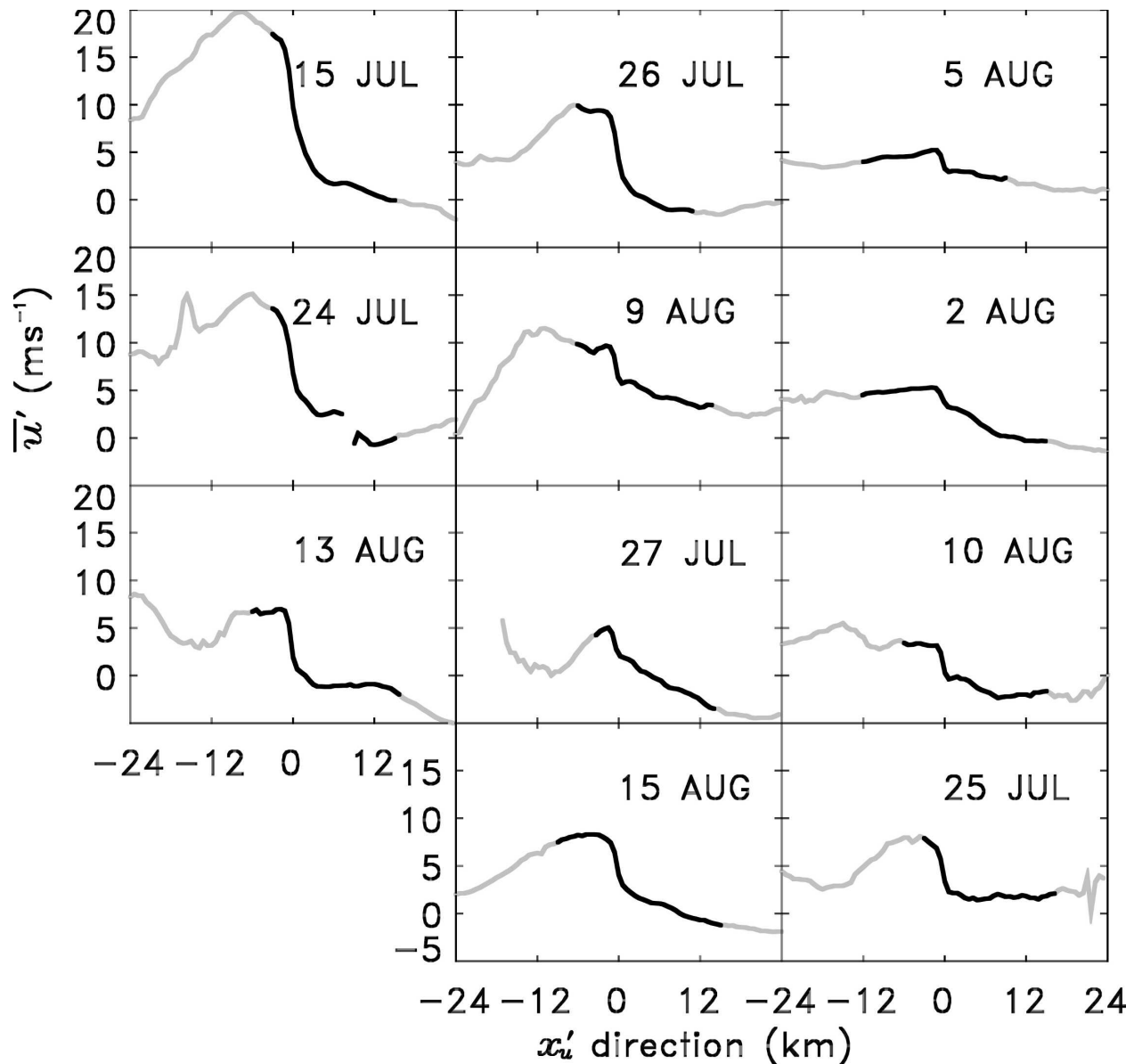


FIG. 10. As in Fig. 9, but for the case-averaged, across-front wind velocity  $u'$  (gray line) shown across the gust front ( $x'_i$  direction). Cases are sorted as in Fig. 9.

a linear fit to the alongfront wind velocities in a fixed 6-km-wide box adjacent to the convergence zone in the postfrontal area. The linear fit is indicated with a gray, dashed line in Fig. 8a. The slope of the linear fit is denoted as  $a_{\text{post}}$ . The difference between  $\bar{v}'$  at the edges of the convergence zone,  $\Delta\bar{v}'_{\text{GF}}$ , is also calculated (Fig. 8a).

The strongest anticyclonic shear was observed on 15 July, identifiable as a rapid decrease of the  $\bar{v}'$  component illustrated in Fig. 9 with  $a_{\text{post}} = -6.1 \text{ m s}^{-1} \text{ per km}$  and  $\Delta\bar{v}'_{\text{GF}} = 10.1 \text{ m s}^{-1}$ . Dominant anticyclonic flow was also found on 13 August with  $a_{\text{post}} = -3.3 \text{ m s}^{-1}$

$\text{km}^{-1}$  and  $\Delta\bar{v}'_{\text{GF}} = 4.9 \text{ m s}^{-1}$ . The influence of misocyclones on the wind field could not be investigated for the 24 July case since the dynamics of the parent thunderstorm affected the postfrontal wind field of the gust front. Based on  $\Delta\bar{v}'_{\text{GF}}$  in Table 3, it appears that the higher the  $\bar{z}_{\text{max}}$ , the stronger the modification of the postfrontal wind field. According to the numerical simulations by LW97a, the observed anticyclonic shear in the postfrontal area close to the convergence might be caused by misocyclones. The amount of anticyclonic shear decreases with misocyclone intensity (Table 3). Anticyclonic shear was detectable on 26 July, 27 July,

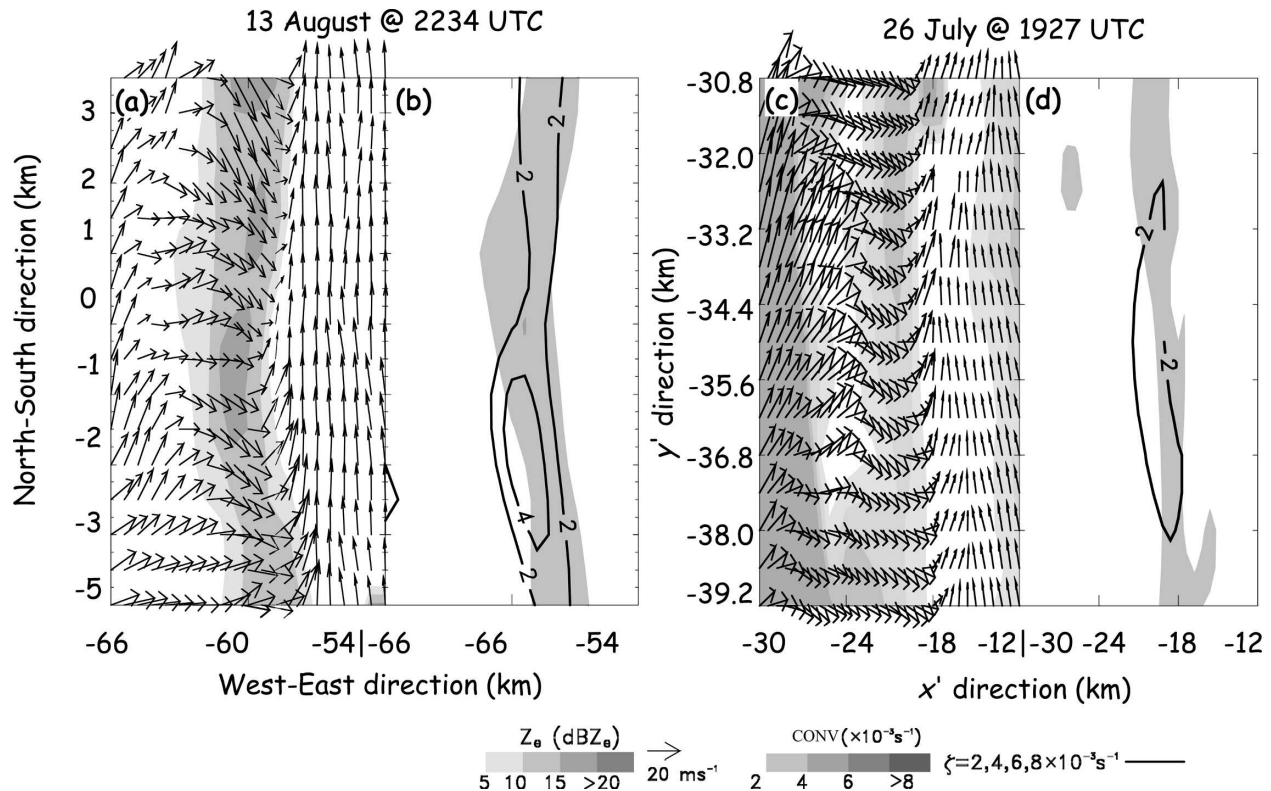


FIG. 11. Close-up view of a part of the convergence zone on (a), (b) 13 Aug and (c), (d) 26 Jul. The horizontal cross sections at 312 m MSL illustrate (a), (c) the horizontal wind field overlaid on the gray-shaded reflectivity factor field (scale at bottom) and (b), (d) vertical vorticity (black lines) overlaid on the gray-shaded convergence field (scaled at bottom) across the gust front ( $x'$  direction). Wind vectors are plotted every 0.6 km.

9 August, and 15 August, but was not evident on 25 July, 2 August, 5 August, and 10 August (Fig. 9, middle and right panels; Table 3). In the latter cases, values of  $a_{\text{post}}$  ranged between  $\pm 1.4 \text{ m s}^{-1}$  per km and  $\Delta \bar{v}'_{\text{GF}} < 2.1 \text{ m s}^{-1}$  (Fig. 9, right panel; Table 3). Based on the methodology for determining wind shear parameters as described in detail in appendix A, weak anticyclonic shear is defined when  $\bar{v}'_{\text{pre-post}}$  and  $\Delta \bar{v}'_{\text{GF}}$  have similar values as on 25 July, 2 August, 5 August, and 10 August.

On 26 July, 27 July, 9 August, and 15 August (middle panel in Fig. 9) two different regimes are shown for the alongfront wind component  $\bar{v}'$ . All four cases have similar values of  $\Delta \bar{v}'_{\text{GF}}$ . In the first regime (27 July, 15 August), the postfrontal wind field is influenced by misocyclones over a shorter distance and  $\bar{v}'_{\text{pre-post}}$  is more pronounced (Table 3). Conversely, the anticyclonic shear is built up over a longer distance, reaching values below  $-4.2 \text{ m s}^{-1}$  per km on 26 July and 9 August (Table 3), even though  $\bar{v}'_{\text{pre-post}}$  is much smaller ( $< 1 \text{ m s}^{-1}$ ) compared to 27 July and 15 August. The horizontal profile of  $\bar{v}'$  on 26 July and 9 August illustrated in Fig. 9 differs from the other CaPE case. This phenomenon is presented in Fig. 11, giving a close-up view

for the wind field across the boundary for 13 August and 26 July. In both cases, misocyclones produced a similar postfrontal anticyclonic shear ( $a_{\text{post}} = -3.3 \text{ m s}^{-1}$  per km for 13 August;  $a_{\text{post}} = -4.2 \text{ m s}^{-1}$  per km for 26 July). The anticyclonic shear developed over a much shorter distance on 13 August (about 3 km) compared to 26 July (about 6 km). Wind shear is much stronger on 13 August compared to 26 July. Based on these horizontal profiles, it can be assumed that strong horizontal wind shear concentrates misocyclone circulation at the gust front. LW97a concluded that the stronger the wind shear, the higher the rate at which lower wavenumber misocyclone patterns are realized (LW97a), so that vertical vorticity can be concentrated more quickly. Therewith, vertical velocity maxima induced by the misocyclone pattern develop at the outflow leading edge.

#### b. Vertical wind shear

The importance of low-level vertical wind shear in modulating the structure of thunderstorm outflows has been investigated in several numerical simulation (e.g., Droegemeier 1985; Rotunno et al. 1988; Lee and Wil-

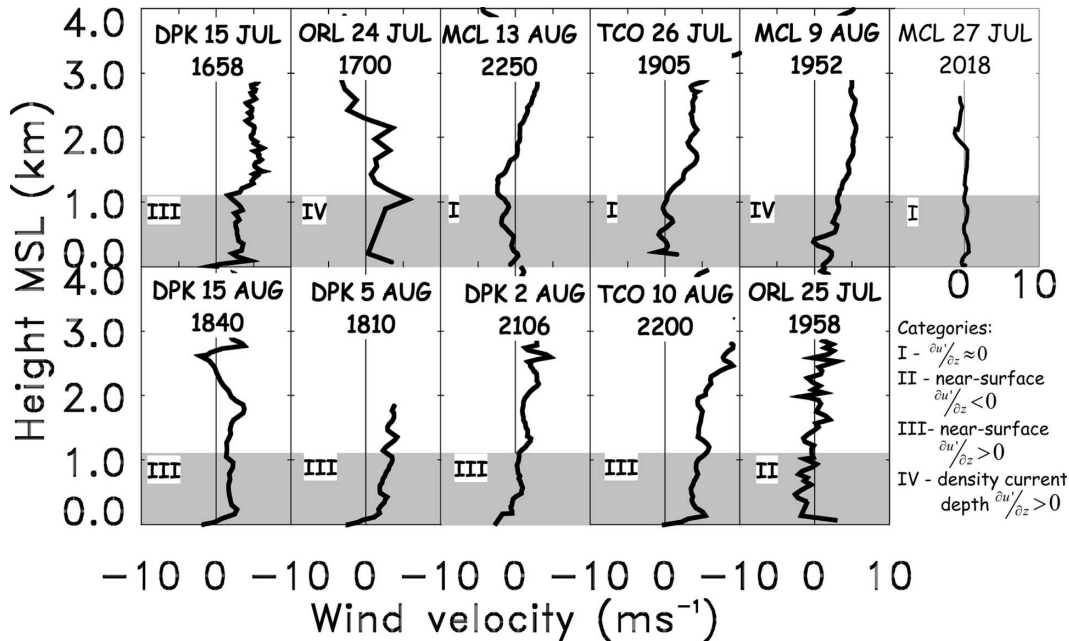


FIG. 12. Vertical profiles of the horizontal wind component ( $\text{m s}^{-1}$ ) orthogonal to the gust front orientation measured by rawinsondes launched in the prefrontal air mass. The assumed mean gust front depth of 1.1 km is shown in gray. Rawinsondes are launched at DPK, ORL, TCO, and MCL. Date and launching time in UTC are indicated. Cases are sorted according to Table 2 starting with the upper-left panel proceeding to the right.

helmson 1997a) and observational (e.g., Wilson and Meigenhardt 1997; Mueller et al. 1993) studies. LW97a suggested that ambient vertical shear directly influences the nose and frontal slope of the outflow leading edge, structures that can impact the development of misocyclones. To place these concepts into the context of CaPE observations, vertical profiles of the horizontal wind in advance of all the gust fronts in this study are presented in Fig. 12. The component of horizontal wind orthogonal to the orientation of each gust front is plotted. The vertical profiles are classified into the four categories defined by LW97a that are based on the strength and vertical extent of shear: 1) no vertical wind shear within the density current depth (26 July, 27 July, 13 August), 2) near-surface negative vertical wind shear (25 July), 3) near-surface positive vertical wind shear (15 July, 2 August, 5 August, 10 August, 15 August), and 4) density current depth positive vertical shear (24 July, 9 August). To compare observational results to numerical simulations, cases are only sorted into one category according to their dominant behavior.

LW97a discovered that simulations with unsheared flows ( $\partial u'/\partial z \approx 0$ ) that opposed the outflow boundary led to less pronounced nose structures and a lack of misocyclone development. However, if the across-front wind component in these unsheared simulations vanished, misocyclone development did occur. These con-

ditions were in place for the 26 July, 27 July, and 13 August CaPE cases where misocyclones with  $1.5 \leq \bar{\zeta}_{\text{max}} \leq 2.5 \times 10^{-3} \text{ s}^{-1}$  were observed. The weakest misocyclone intensity ( $\bar{\zeta}_{\text{max}} \leq 0.7 \times 10^{-3} \text{ s}^{-1}$ ) was evident on 25 July in association with near-surface negative vertical wind shear ( $\partial u'/\partial z < 0$ ). LW97a found no discernable nose structure at the leading edge of outflows simulated under these conditions. As a result, lobe-and-cleft instabilities did not form and were not available to trigger horizontal shear instabilities that could eventually form misocyclones. In contrast, LW97a found that highly exaggerated nose structures developed in simulations with positive vertical wind shear ( $\partial u'/\partial z > 0$ ), and, in these cases, misocyclones developed. Positive vertical wind shear profiles (categories III and IV in Fig. 12) were in place for seven of the CaPE cases (15 July, 24 July, 2 August, 5 August, 9 August, 10 August, and 15 August). Misocyclone intensities in these cases ranged from  $\bar{\zeta}_{\text{max}} = 1 \times 10^{-3} \text{ s}^{-1}$  on 10 August to  $\bar{\zeta}_{\text{max}} = 4.4 \times 10^{-3} \text{ s}^{-1}$  on 15 July. LW97a concluded that stronger misocyclones form when the depth of positive vertical wind shear is comparable to the depth of the outflow boundary and balanced with the buoyantly generated, oppositely directed vertical shear of the cold pool. This conclusion is based upon and is closely related to the hypotheses of Rotunno et al. (1988) that involve the relative balance of horizontal vorticity be-

tween cold pools and their ambient environment and the impact of this balance on the slope of resulting updrafts and the intensity and longevity of convection that develops. It was not possible to determine the specific depth of each outflow boundary in this study. Since the same analysis strategy is applied to all cases, an average depth of 1.1 km was assumed for each gust front based on the studies of Atkins and Wakimoto (1997) and Kingsmill and Crook (2003). Note that although both studies derive the same average gust front depth, individual gust front depths vary between 200 and 800 m. In our study, vertical shear calculated over the depth of the gust front varied by an average of about  $1.5 \text{ m s}^{-1}$  when the assumed depth varied from 0.6 to 1.6 km. Unlike the environment ahead of the CaPE gust fronts, information to characterize the vertical shear profile in the cold pool behind the gust fronts is very limited. Therefore, to assess the relative balance of horizontal vorticity in each case, we employ the methodology used by Rotunno et al. (1988), which essentially compares the difference in horizontal wind speeds orthogonal to, ahead, and over the depth of the gust front with the propagation speed of the gust front [i.e., their Eq. (10)]. Rotunno et al. (1988) claim that when these parameters are comparable, an optimal horizontal vorticity balance is in effect. For example, they used this approach to assert an optimal horizontal vorticity balance in the case observed by Carbone (1982).

A direct comparison of gust front propagation speed ( $\overline{UP}_{SPD}$ ) and the difference in horizontal wind speed orthogonal to, ahead, and over the assumed depth of the gust fronts ( $\Delta u'$ ) is provided in Fig. 13. Most of the cases show that the implied horizontal vorticity in the cold pool circulation dominates the circulation in the environment ahead of the gust front. However, the 2 August case is close to optimally balanced, with absolute differences between and less than  $1 \text{ m s}^{-1}$ . The shear in the ambient environment extends through the assumed depth of the gust front, the optimal condition for misocyclone development asserted by LW97a. These optimal conditions were associated with only a few, relatively weak ( $\tilde{\zeta}_{\max} = 1 \times 10^{-3} \text{ s}^{-1}$ ) misocyclones. Although variations in the assumed gust front depth lead to different  $\Delta u'$ , these changes do not lead to significant differences in the nature of the horizontal vorticity balance between gust front cold pools and their ambient environments.

In most of the cases, wind shear in the ambient environment ahead of the gust front is very weak, so that the cold pool circulation within the gust front dominates. Conditions close to optimally balanced were only observed in one case, with only a few weak misocyclones.

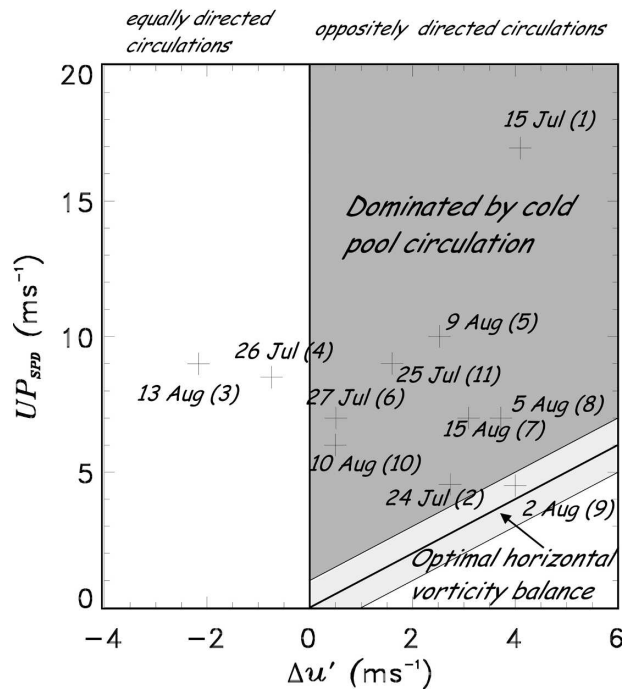


FIG. 13. A comparison of gust front propagation speed ( $\overline{UP}_{SPD}$ ) with the difference in horizontal wind speed orthogonal to, ahead of, and over the assumed depth of the gust front ( $\Delta u'$ ) for the purpose of asserting the relative balance of horizontal vorticity between the cold pool and the ambient environment. Number in brackets indicates the order of misocyclone intensity according to Table 2.

clones. As a result, the impact of vertical wind shear on misocyclone intensity as concluded by LW97a was not evident in the Florida gust fronts observed during CaPE.

### c. Static stability

LW97a also proposed that an environment as close as possible to neutrally stable through a layer considerably deeper than the outflow boundary was optimal for the development of strong misocyclone circulations. In their simulations the neutrally stable layer is about 57% deeper than the gust front depth. To test this result with observations, vertical profiles of potential temperature ahead of all the CaPE gust front cases are now examined (Fig. 14). Following LW97a, a neutrally stable layer of 1.65-km depth must exist in order to have an optimal environment for misocyclones. This value is related to a 50% increase in the average gust front depth. Optimal static stability for strong misocyclone development (category I in Fig. 14) was found on 25 July, 26 July, 27 July, 2 August, 5 August, 10 August, and 15 August. However, misocyclone intensity in these cases varied between  $1 \leq \tilde{\zeta}_{\max} \leq 1.6 \times 10^{-3} \text{ s}^{-1}$ . Most

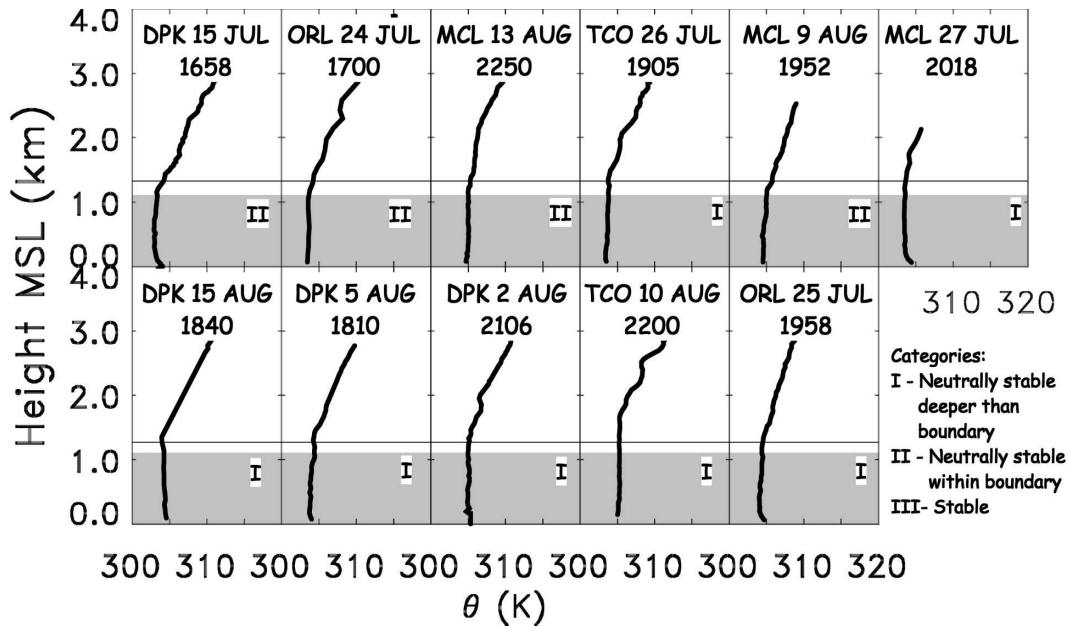


FIG. 14. Vertical profiles of potential temperature measured by rawinsondes launched ahead of the gust front at ORL, DPK, TCO, and MCL. The assumed mean boundary depth of 1.1 km is shown in gray. Date and launching time in UTC are indicated. The level 50% higher than the assumed mean boundary depth is at 1.65 km and indicated by a horizontal, thin black line. Cases are sorted according to Table 2 starting with the upper-left panel proceeding to the right.

of the remaining cases have a neutrally stable layer, but it is not considerably deeper than the outflow (category II in Fig. 14). Misocyclone intensity in these cases also varies widely, with  $\bar{\zeta}_{\max} = 1.5 \times 10^{-3} \text{ s}^{-1}$  on 9 August and  $\bar{\zeta}_{\max} = 4.4 \times 10^{-3} \text{ s}^{-1}$  on 15 July. Therefore, in contrast to the conclusions of LW97a, the observed static stability in advance of the gust fronts in this study does not appear to show any correlation with the intensity of misocyclone circulations.

### 5. Influence of misocyclones on convection initiation

The occurrence of misocyclones and their possible spatial relationship to convective cell initiation are compared. The results of this analysis are listed in Table 4. Misocyclone occurrence is investigated based on multiple-Doppler-derived wind fields available at the analysis times. With an average interval between analysis times of about 15 min, temporal tracking of misocyclones is not feasible. The analysis of convection initiation is based on reflectivity factor measurements from CP4 or CP3 available at a higher temporal resolution of about 5 to 10 min. CP3 measurements were only applied when CP4 was either not in operation as on 15 August or its reflectivity values were biased as on 15 July. Convection initiation is defined in the same

manner as that of Wilson and Schreiber (1986): newly developed precipitation areas that have a reflectivity core higher than 30 dBZ and are not attached to existing storms. For each case, convection is tracked from the first multiple-Doppler analysis time (Fig. 2) until 10 min after the last multiple-Doppler analysis time unless collision of the gust front with a sea-breeze front is

TABLE 4. Convection initiation (CI) occurrence, either single cell or multiple cell (“x”), and its relationship to misocyclones (MC). When no linkage between convection initiation and misocyclones was found, cases are labeled as “No MC/CI,” while “Ana imposs” indicates that an analysis is not possible due to insufficient temporal and spatial Doppler radar coverage. Convection was not initiated in cases marked as “No CI.” Case ordering and bold highlighting as in Table 2.

Date	Single-cell CI	Multiple-cell CI	CI and MC
15 Jul			Ana imposs
24 Jul			Ana imposs
<b>13 Aug</b>	x		Ana imposs
<b>26 Jul</b>	x		No MC/CI
9 Aug			No CI
<b>27 Jul</b>		x	No MC/CI
<b>15 Aug</b>		x	No MC/CI
5 Aug			No CI
<b>2 Aug</b>		x	No MC/CI
<b>10 Aug</b>	x		Ana imposs
<b>25 Jul</b>		x	No MC/CI

imminent, at which point the tracking analysis is terminated. In addition, convection initiation is tracked only within the segmental areas (i.e., section 4a, Fig. 3) employed for a particular case. Note that for certain analysis times, determination of convection initiation and its possible relationship to misocyclones is not possible due to insufficient temporal and spatial coverage of multiple-Doppler-derived wind fields.

Convection initiation was clearly observed in 7 of the 11 cases (Table 4). For these seven cases, the relationship between initiated convection and misocyclones is separated into three categories. The first category is composed of those cases where newly developed convective cells are located within 6 km of the misocyclone center. This distance represents a length scale that is approximately 3 times the maximum radius of a misocyclone. In the second category, convection initiates outside the 6-km range centered on the misocyclone. These cases are treated as if there is no spatial relationship between newly developed convective cells and misocyclones. The third category consists of cases where an analysis was impossible due to insufficient temporal and spatial coverage of multiple-Doppler-derived winds or ambiguous reflectivity structures for determining if newly developed cells have formed.

In five of the seven cases with convection initiation, none of the local maxima of vertical vorticity and convergence was observed to be a preferred area of development for new convective cells. As an example, Fig. 15 shows the spatial and temporal evolution of vertical vorticity and convergence together with the locations of convection initiation for the case on 2 August. Convection is initiated along and behind the gust front mainly in the northern part of the domain (Figs. 15a,c,e). A misocyclone along the gust front was first observed at 2129 UTC and is indicated by a square in Fig. 15b. In the analysis times that follow at 2144 and 2159 UTC, no convection was initiated in the vicinity of this misocyclone, indicated by squares in Figs. 15c and 15d. Also in the vicinity of a second misocyclone at 2144 UTC, indicated by the circle in Fig. 15d, no newly developed areas of enhanced reflectivity were observed (Fig. 15e). Note that Fig. 15 only shows the reflectivity at 300 m AGL, while the analysis focuses also on higher-elevation angles. The misocyclone that developed at 2159 UTC along the gust front position at 2129 UTC (along the dashed line in Fig. 15f) is related to the convective cell that formed at 2144 UTC (Fig. 15c) and cannot be related to the gust front.

Analysis of the relationship between misocyclones and convection initiation is not possible on 10 and 13 August because of insufficient temporal and spatial

coverage of multiple-Doppler data. When the thunderstorms that produce or maintain a gust front are very close to the trailing edge of a boundary, it is not possible to unambiguously determine if new convection is initiated based on radar reflectivity, a complication that was evident on 15 and 24 July. Convection initiation was definitely not observed on 5 and 9 August. As a result, establishing a spatial linkage between misocyclones and convection initiation was not possible in these cases.

## 6. Conclusions

Misocyclone characteristics along 11 gust fronts observed in Florida during the CaPE project have been examined with multiple-Doppler radar and rawinsonde data. The investigation focused on three main issues: 1) the intensity range of misocyclones and their organization along the gust front, especially with respect to convergence; 2) the relationship between misocyclone intensity and horizontal wind shear, vertical wind shear, and static stability; and 3) the relationship between misocyclones and convection initiation.

The intensity of misocyclones, as indicated by maximum values of vertical vorticity ( $\zeta_{\max}$ ), varied from  $2.8 \times 10^{-3}$  to  $13.9 \times 10^{-3} \text{ s}^{-1}$ , although all but one case (15 July) exhibited values less than  $6.4 \times 10^{-3} \text{ s}^{-1}$  (Table 2). These values are based on multiple-Doppler analyses with a resolvable wavelength of 3.6 km.

The organization of misocyclones and associated kinematic structures is summarized in a conceptual model (Fig. 16). Note how this model differs from the conceptual model for misocyclone development based on the numerical simulation results of LW97a presented in Fig. 1. For example, there were organized patterns of misocyclones with 3–7-km spacing, but they were usually only evident along small segments of a gust front (Fig. 16). Also, the position of convergence maxima relative to misocyclones was inconsistent; some convergence maxima were on one side of a misocyclone, some were on both sides, while others were nearly collocated. The influence of resolvable wavelength on these results has to be investigated using higher-resolution observations. The CaPE observations also indicate that pre- and postfrontal winds vary in speed and direction along the boundary, a deviation from the LW97a conceptual model. In addition, cases with relatively strong misocyclones ( $\zeta_{\max} > 4 \times 10^{-3} \text{ s}^{-1}$ ) showed an anticyclonic shear in the postfrontal winds—a phenomenon well simulated by LW97a.

The optimal environmental conditions for misocyclone development proposed by LW97a were assessed

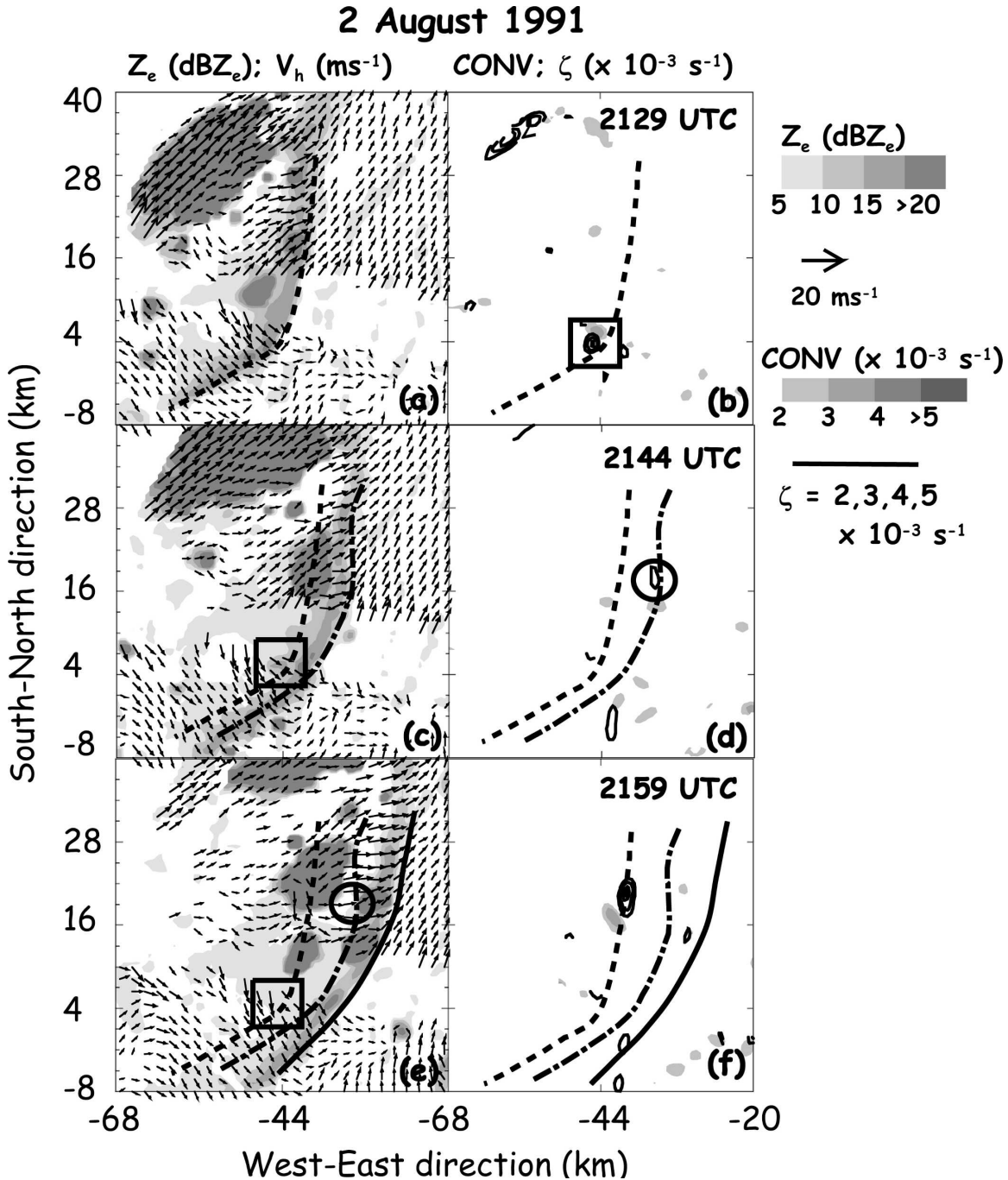


FIG. 15. Horizontal cross sections of multiple-Doppler-derived data at 312 m MSL for (a), (b) 2129, (c), (d) 2144, and (e), (f) 2159 UTC on 2 Aug. (left) Horizontal winds (arrows) are overlaid on gray-shaded reflectivity (scale on the right), while (right) positive vertical vorticity (black contours) is overlaid on gray-shaded convergence (scale on the right). The location of a misocyclone first observed at 2129 UTC is indicated by a square [(b), (c), (e)], while the location of a misocyclone first observed at 2144 UTC is indicated by a circle [(d), (e)]. The location of the leading edge of the gust front is indicated at 2129 UTC as a dashed line, at 2144 UTC as a dashed-dotted line, and at 2159 UTC as a solid line, respectively.

observationally by examining the relationship between misocyclone intensity and horizontal wind shear, vertical wind shear, and static stability. Results are summarized in Table 5. Misocyclone intensity was found to be

most closely linked to the strength of horizontal wind shear. This result validates the hypothesis by Kingsmill (1995). When the component of alongfront wind differed by more than  $4 \text{ m s}^{-1}$  in the pre- and postfrontal

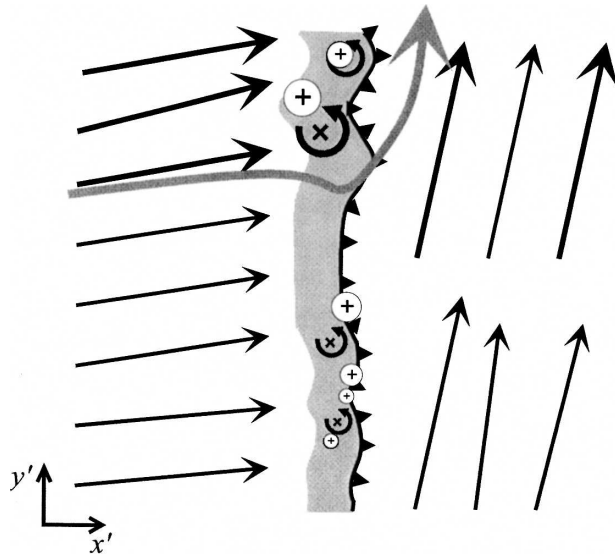


FIG. 16. Schematic diagram combining the results of this study with the conceptual model for misocyclone circulation along the leading edge of thunderstorm outflows portrayed in Fig. 1. The thick gray arrow indicates the influence of misocyclones on the horizontal wind field. Sizes of convergence and vertical vorticity symbols are scaled to their intensity; magnitude of the wind vector is related to its thickness. Areas of enhanced positive vertical vorticity are indicated with crosses and areas of convergence with plus signs. The convergence zone is highlighted in gray.

air masses, misocyclones with  $\bar{\zeta}_{\max} > 2.5 \times 10^{-3} \text{ s}^{-1}$  were observed. The linkage between misocyclone intensity and vertical wind shear and static stability was much less clear. For optimal misocyclone development, LW97a concluded that the prefrontal air mass needed

TABLE 5. Occurrence of environmental conditions hypothesized by LW97a to be optimal for producing strong misocyclones. Highlighted cases ("x") have a strong across-front horizontal wind shear defined as  $\bar{v}'_{\text{pre-post}} > 4 \text{ m s}^{-1}$ , a prefrontal vertical shear profile of depth similar to the outflow and balanced with cold pool circulation, and/or an environment close to neutrally stable through a layer 50% deeper than the outflow boundary. Case ordering and bold highlighting as in Table 2.

Date	Horizontal wind shear	Vertical wind shear	Static stability
15 Jul	x		
24 Jul	x		
<b>13 Aug</b>	x		
<b>26 Jul</b>			x
9 Aug			
<b>27 Jul</b>			x
<b>15 Aug</b>			x
5 Aug			x
<b>2 Aug</b>		x	x
<b>10 Aug</b>			x
<b>25 Jul</b>			x

to be close to neutrally stable throughout a layer considerably deeper than the boundary, and its vertical shear needed to extend throughout the depth and balance the cold pool circulation of the gust front. The static stability condition was satisfied in seven cases, which occurred in association with  $0.7 \leq \bar{\zeta}_{\max} \leq 1.6 \times 10^{-3} \text{ s}^{-1}$ . In contrast, the vertical shear condition was satisfied in only one case. However, this case was associated with very weak misocyclones ( $\bar{\zeta}_{\max} = 1 \times 10^{-3} \text{ s}^{-1}$ ), thus confuting the vertical shear portion of the LW97a hypothesis.

Finally, the spatial and temporal linkage between misocyclones and convection initiation were investigated. Of the 11 gust front cases analyzed, 7 were associated with the initiation of convection. Spatial-temporal relationships between misocyclones and convection initiation were not evident in any of these cases.

This study is unique because it examines observations of misocyclone development for several cases within the same region (i.e., Florida). The wider geographic applicability of the results is not certain. For example, other locales in the United States, such as the central plains, have different topographic features, environmental characteristics (e.g., vertical wind shear, static stability), and a wider array of boundary types (e.g., cold fronts, drylines, gust fronts) oriented and propagating in a wider range of directions. These factors may combine to produce different misocyclone structures and relationships to environmental characteristics. Observations from the May–June 2002 International H2O Project (IHOP) may provide an opportunity to address these issues.

*Acknowledgments.* We extend special thanks to Janet Intrieri, NOAA; Al Bedard, NOAA; Tammy Weckwerth, NCAR; Jim Wilson, NCAR; and the two anonymous reviewers for providing comments and suggestions that enhanced the quality of the paper. The authors thank Bob Rilling of NCAR for assisting in the acquisition of CP3, CP4, and CLASS data. FL2 and UND data were provided by Deborah Diskin of the MIT Lincoln Laboratory under sponsorship from the Federal Aviation Administration. Editing and interpolation of radar data was performed using the SOLO and REORDER programs developed by the Earth Observing Laboratory of NCAR. Dual-Doppler analyses were performed using the CEDRIC program developed by the Mesoscale and Microscale Meteorology Division of NCAR. Ming Xiao and Sean Wilson of DRI assisted with the editing and analysis of radar data. This research was sponsored by the National Science Foundation under Grants ATM-9901688 and ATM-0432951.

## APPENDIX A

**Methodology for Determining Horizontal Wind Shear Parameters**

Across- and alongfront wind velocities within the rotated coordinate system (denoted as  $u'$  and  $v'$  component) are averaged in the  $x'$  direction along all cross sections per segment  $y'$ , all segments per analysis time  $S$ , and all analysis times per case  $t$  as

$$\overline{u'}, \overline{v'}(x', y') = \underbrace{\frac{1}{p} \sum_{k=t_0}^{t_p} \frac{1}{m} \sum_{j=S_1(k)}^{s_m(k)} \underbrace{\frac{1}{n} \sum_{i=y_1(j,k)}^{y_n(j,k)} u', v'(x', y')}_{\text{Segmental average}}}_{\text{Temporal average}}_{\text{Case average}} \quad (\text{A1})$$

The number of cross sections per segment is denoted as  $n$ , number of segments per analysis time as  $m$ , and number of analysis times per case as  $p$ . The number of analysis times per case ranged between one (e.g., 25 July) and five (e.g., 5 and 15 August). The number of cross sections per analysis time varied between 40 (e.g., 24 and 27 July) and 180 (e.g., 26 July). First, the segmental average of  $u'$  is achieved by spatially shifting each individual cross section along the  $x'$  direction in a manner such that the maximum values of  $\partial u'/\partial x'$  within the 6-km-wide gust front box are aligned with each other. For the  $v'$  component, the absolute minimum values of  $v'$  within the 6-km-wide gust front box along each cross section are aligned with each other. An example of this procedure is given in Fig. 8 showing the segmental average of  $v'$  and  $u'$  along the  $x'$  direction for the northern segment on 13 August, illustrated in Fig. 4b (denoted as box C). The location of the maximum value of  $\partial u'/\partial x'$  and the minimum value of  $v'$  is denoted as  $x'_u = x'_v = 0$  in Fig. 8.

The width of the convergence zone along gust fronts is variable in time and space. To avoid overly smoothing the variations in  $u'$  and  $v'$  through the temporal and case-averaging processes, the segmentally averaged across- and alongfront wind components are used to calculate horizontal wind shear parameters for each segment. For the analysis these parameters are averaged over all segments of a particular analysis time and over all analysis times. The strength of horizontal wind shear is defined by wind characteristics in the post- and prefrontal areas that are adjacent to the convergence zone as shown in Fig. 8. Thus, the width of the convergence zone is determined for each segment separately. It is defined as the area around  $x'_u = 0$  having a gradient of  $\partial u'/\partial x'$  larger than  $0.2 \text{ s}^{-1}$ . This threshold is chosen

empirically based on the typical shape of the segmental average of  $u'$  for all cases. The width of the convergence zone sometimes exceeds 6 km when applying this threshold. In these cases, the width is reset to 6 km. This defined convergence zone is then used as an anchor in the analysis of  $v'$  components. Based on examination of all cases, the postfrontal edge of the convergence zone resides at the location of the minimum value of  $v'$  ( $x'_v = 0$ ). The prefrontal edge of the convergence zone is then located a distance equal to the convergence zone width toward the prefrontal domain. For example, the convergence zone has a width of 4.2 km and is located between  $-2.4 \text{ km} \leq x'_u \leq 1.8 \text{ km}$  in Fig. 8b, and the convergence zone for the corresponding alongfront wind component is located between  $0 \text{ km} \leq x'_v \leq 4.2 \text{ km}$  in Fig. 8a. For all of the analyzed CaPE cases, the width of the convergence zone ranges from 1.8 km in the southern segment at 1819 UTC on 5 August up to 6 km in the southern segment at 2159 UTC on 2 August.

The adjacent post- and prefrontal areas are defined according to the width of the convergence zone. Generally, the postfrontal area is defined as 12 km behind the convergence zone, while the prefrontal area is 12 km ahead. When large parts of the parent thunderstorm or the sea-breeze front influence the wind field in these 12-km-wide boxes, the width is reduced. In Fig. 8 the width of the postfrontal box is reduced to 6 km since the wind field of the parent thunderstorm located in the southwest corner of the 12-km-wide postfrontal box (Fig. 3b) influences the segmental average of  $u'$  and  $v'$  (Fig. 8).

Postfrontal, anticyclonic shear of the  $\overline{v'}$  component close to the convergence zone is quantified by the slope value,  $a_{\text{post}}$ , and the difference of  $\overline{v'}$  within the convergence zone, denoted as  $\Delta \overline{v'}_{\text{GF}}$ , in Table 3. Note that when analyzing anticyclonic shear in the postfrontal area, a constant 6-km width is applied to all cases. This can yield to underestimation of  $a_{\text{post}}$ , since the anticyclonic shear is sometimes only evident within 3 km of the convergence zone such as observed on 15 July. Anticyclonic shear can also extend the full distance of 6 km as on 9 August (Fig. 9). In both cases a slope value of about  $6 \text{ m s}^{-1} \text{ per km}$  is determined (Table 2). With the combination of  $a_{\text{post}}$  and  $\Delta \overline{v'}_{\text{GF}}$ , a clearer statement about the strength of anticyclonic shear and the distance of its influence relative to the convergence zone is possible. Since  $\Delta \overline{v'}_{\text{GF}}$  is much larger on 15 July ( $10.1 \text{ m s}^{-1}$ ) than on 9 August ( $3.1 \text{ m s}^{-1}$ ), stronger anticyclonic shear over a shorter distance occurred on 15 July. Anticyclonic shear across the full 6-km width was only observed on 26 July and 9 August. For all other cases, wind fields are modified within less than 3 km behind the convergence zone (Fig. 9).

## APPENDIX B

## List of Symbols

Parameter	Definition
CONV	Convergence
$\overline{\text{CONV}}_{\text{max}}$	Average maximum convergence
$\text{CONV}_{\text{max}}$	Maximum convergence
S	Segment per analysis time
$\overline{UP}_{\text{DIR}}$	Gust front propagation direction
$\overline{UP}_{\text{SPD}}$	Gust front propagation speed
$a_{\text{post}}$	Postfrontal, anticyclonic shear parameter
m	Number of segments per analysis time
n	Number of cross sections per segment
p	Number of analysis times per case
t	Analysis time per case
u	Wind velocity in west–east direction
$u'$	Wind velocity orthogonal to the gust front
$\overline{u'}$	Case average across-front wind velocity
$\overline{u'}_{\text{post}}$	Mean postfrontal, across-front wind velocity
$\overline{u'}_{\text{pre}}$	Mean prefrontal, across-front wind velocity
$\overline{u'}_{\text{post-pre}}$	Difference between $\overline{u'}_{\text{post}}$ and $\overline{u'}_{\text{pre}}$
$\Delta u'$	Horizontal wind speed orthogonal to, ahead of, and over the assumed depth of the gust front
v	Wind velocity in south–north direction
$v'$	Wind velocity parallel to the gust front
$\overline{v'}$	Case average alongfront wind velocity
$\Delta \overline{v'}_{\text{GF}}$	Difference between $\overline{v'}$ at the edges of the convergence zone
$\overline{v'}_{\text{post}}$	Mean postfrontal, alongfront wind velocity
$\overline{v'}_{\text{pre}}$	Mean prefrontal, alongfront wind velocity
$\overline{v'}_{\text{pre-post}}$	Difference between $\overline{v'}_{\text{pre}}$ and $\overline{v'}_{\text{post}}$
x	Axis in south–north direction
$x'$	Axis orthogonal to the gust front
y	Axis in west–east direction
$y'$	Axis parallel to the gust front
$\Delta y'$	Length of the analyzed gust front
$\zeta$	Vertical vorticity
$\overline{\zeta}_{\text{max}}$	Average maximum vertical vorticity
$\zeta_{\text{max}}$	Maximum vertical vorticity

## REFERENCES

- Arnott, N. R., and Y. P. Richardson, 2004: High resolution observations of a cold front on 10 June 2002. Preprints, *22d Conf. on Severe Local Storms*, Hyannis, MA, Amer. Meteor. Soc., CD-ROM, 16A.3.
- , —, J. M. Wurman, and E. M. Rasmussen, 2005: Relationship between a weakening cold front, mesocyclones, and cloud development on 10 June 2002 during IHOP. *Mon. Wea. Rev.*, in press.
- Atkins, N. T., and R. M. Wakimoto, 1997: Influence of the synoptic-scale flow on sea breezes observed during CaPE. *Mon. Wea. Rev.*, **125**, 2112–2130.
- , —, and T. M. Weckwerth, 1995: Observations of the sea-breeze front during CaPE. Part II: Dual-Doppler and aircraft analysis. *Mon. Wea. Rev.*, **123**, 944–969.
- , —, and C. L. Ziegler, 1998: Observations of the finescale structure of a dryline during VORTEX 95. *Mon. Wea. Rev.*, **126**, 525–550.
- Carbone, R. E., 1982: A severe frontal rainband. Part I: Storm-wide hydrodynamic structure. *J. Atmos. Sci.*, **39**, 258–279.
- , 1983: A severe frontal rainband. Part II: Tornado parent vortex circulation. *J. Atmos. Sci.*, **40**, 2639–2654.
- , M. J. Carpenter, and C. D. Burghart, 1985: Doppler radar sampling limitations in convective storms. *J. Atmos. Oceanic Technol.*, **2**, 357–361.
- , J. W. Conway, N. A. Crook, and M. W. Moncrieff, 1990: The generation and propagation of nocturnal squall line. Part I: Observations and implications for mesoscale predictability. *Mon. Wea. Rev.*, **118**, 26–49.
- Cressman, G. P., 1959: An operational objective analysis system. *Mon. Wea. Rev.*, **87**, 367–374.
- Droegemeier, K. K., 1985: *The Numerical Simulation of Thunderstorm Outflow Dynamics*. Ph.D. dissertation, University of Illinois at Urbana–Champaign, 695 pp.
- Frankhauser, J. C., N. A. Crook, J. Tuttle, L. J. Miller, and C. G. Wade, 1995: Initiation of deep convection along boundary layer convergence lines in a semitropical environment. *Mon. Wea. Rev.*, **123**, 291–313.
- Fujita, T. T., 1981: Tornadoes and downbursts in the context of generalized planetary scales. *J. Atmos. Sci.*, **38**, 1511–1534.
- Kingsmill, D. E., 1995: Convection initiation associated with a sea-breeze front, a gust front, and their collision. *Mon. Wea. Rev.*, **123**, 2913–2933.
- , and N. A. Crook, 2003: An observational study of atmospheric bore formation from colliding density currents. *Mon. Wea. Rev.*, **131**, 2985–3002.
- Laird, N. F., D. A. R. Kristovich, R. M. Rauber, H. T. Ochs, and L. J. Miller, 1995: The Cape Canaveral sea and river breezes: Kinematic structure and convective initiation. *Mon. Wea. Rev.*, **123**, 2942–2956.
- Lee, B. D., and R. B. Wilhelmson, 1997a: The numerical simulation of non-supercell tornadogenesis. Part I: Initiation and evolution of pretornadic mesocyclone circulation along a dry outflow boundary. *J. Atmos. Sci.*, **54**, 32–60.
- , and —, 1997b: The numerical simulation of non-supercell tornadogenesis. Part II: Evolution of a family of tornadoes along a weak outflow boundary. *J. Atmos. Sci.*, **54**, 2387–2415.
- Marquis, J. N., and Y. P. Richardson, 2004: Observations of mesocyclones along boundaries during IHOP. Preprints, *22d Conf. on Severe Local Storms*, Hyannis, MA, Amer. Meteor. Soc., CD-ROM, 16A.5.
- Mueller, C. K., and R. E. Carbone, 1987: Dynamics of a thunderstorm outflow. *J. Atmos. Sci.*, **44**, 1879–1898.
- , J. W. Wilson, and N. A. Crook, 1993: The utility of sounding and mesonet data to nowcast thunderstorm initiation. *Wea. Forecasting*, **8**, 132–146.
- Murphey, H. V., R. M. Wakimoto, C. Flamant, and D. E. Kingsmill, 2005: Dryline on 19 June 2002 during IHOP. Part I: Airborne Doppler and LEANDRE II analyses of the thin line structure and convection initiation. *Mon. Wea. Rev.*, in press.
- Neumann, J., 1951: Land breezes and nocturnal thunderstorms. *J. Meteor.*, **8**, 60–67.
- Pielke, R. A., 1974: A three-dimensional numerical model of the sea-breezes over south Florida. *Mon. Wea. Rev.*, **102**, 115–139.

- Purdum, J. F. W., 1976: Some uses of high-resolution GOES imagery in the mesoscale forecasting of convection and its behavior. *Mon. Wea. Rev.*, **104**, 1474–1483.
- , 1982: Subjective interpretation of geostationary satellite data for nowcasting. *Nowcasting*, K. Browning, Ed., Academic Press, 149–166.
- Rotunno, R., J. B. Klemp, and M. L. Weisman, 1988: A theory for strong, long-lived squall lines. *J. Atmos. Sci.*, **45**, 463–485.
- Wakimoto, R. M., and J. W. Wilson, 1989: Non-supercell tornadoes. *Mon. Wea. Rev.*, **117**, 1113–1140.
- , and J. K. Lew, 1993: Observation of a Florida waterspout during CaPE. *Wea. Forecasting*, **8**, 412–423.
- , and N. T. Atkins, 1994: Observations of the sea-breeze front during CaPE. Part I: Single-Doppler, satellite, and cloud photogrammetric analysis. *Mon. Wea. Rev.*, **122**, 1092–1114.
- , and D. E. Kingsmill, 1995: Structure of an atmospheric undular bore generated from colliding boundaries during CaPE. *Mon. Wea. Rev.*, **123**, 1374–1393.
- Weckwerth, T. M., 2000: The effect of small-scale moisture variability on thunderstorm initiation. *Mon. Wea. Rev.*, **128**, 4017–4030.
- , and R. M. Wakimoto, 1992: The initiation and organization of convective cells atop a cold-air outflow boundary. *Mon. Wea. Rev.*, **120**, 2169–2187.
- , J. W. Wilson, and R. M. Wakimoto, 1996: Thermodynamic and variability within the boundary layer due to horizontal convective rolls. *Mon. Wea. Rev.*, **124**, 769–784.
- Wilson, J. W., and W. E. Schreiber, 1986: Initiation of convective storms at radar-observed boundary-layer convergence lines. *Mon. Wea. Rev.*, **114**, 2516–2536.
- , and D. L. Megenhardt, 1997: Thunderstorm initiation, organization, and lifetime associated with Florida boundary layer convergence lines. *Mon. Wea. Rev.*, **125**, 1507–1525.
- , G. B. Foote, N. A. Crook, J. C. Frankhauser, C. G. Wade, J. D. Tuttle, C. K. Mueller, and S. K. Krueger, 1992: The role of the boundary-layer convergence zones and horizontal rolls in the initiation of thunderstorms: A case study. *Mon. Wea. Rev.*, **120**, 1785–1815.
- Yuter, S. E., and R. A. Houze, 1995: Three-dimensional kinematic and microphysical evolution of Florida cumulonimbus. Part I: Spatial distribution of updraft, downdraft, and precipitation. *Mon. Wea. Rev.*, **123**, 1921–1940.